



— BUREAU OF —
RECLAMATION

**Desalination and Water Purification Research
and Development Program Report No. 232**

Model-Guided Optimal Design and Fabrication of an Integrated Solar- Driven Hollow Fiber Membrane Distillation Module

**U.S. Department of the Interior
Bureau of Reclamation
Technical Service Center
Denver, Colorado**

August 2021

REPORT DOCUMENTATION PAGE			Form Approved OMB No. 0704-0188		
<p>The public reporting burden for this collection of information is estimated to average 1 hour per response, including the time for reviewing instructions, searching existing data sources, gathering and maintaining the data needed, and completing and reviewing the collection of information. Send comments regarding this burden estimate or any other aspect of this collection of information, including suggestions for reducing the burden, to Department of Defense, Washington Headquarters Services, Directorate for Information Operations and Reports (0704-0188), 1215 Jefferson Davis Highway, Suite 1204, Arlington, VA 22202-4302. Respondents should be aware that notwithstanding any other provision of law, no person shall be subject to any penalty for failing to comply with a collection of information if it does not display a currently valid OMB control number.</p> <p>PLEASE DO NOT RETURN YOUR FORM TO THE ABOVE ADDRESS.</p>					
1. REPORT DATE (DD-MM-YYYY) 08-10-2021		2. REPORT TYPE Final		3. DATES COVERED (From - To) 02/08/2017-12/31/2019	
4. TITLE AND SUBTITLE Model-Guided Optimal Design and Fabrication of an Integrated Solar-Driven Hollow Fiber Membrane Distillation Module			5a. CONTRACT NUMBER Agreement No. R17AC00139		
			5b. GRANT NUMBER		
6. AUTHOR(S) Siamak Nejati, Assistant Professor Mona Bavarian, Assistant Professor Mahdi Mohammadi Ghaleni, Ph.D. Student Abdullah Al Balushi, Graduate Student			5c. PROGRAM ELEMENT NUMBER		
			5d. PROJECT NUMBER		
7. PERFORMING ORGANIZATION NAME(S) AND ADDRESS(ES) University of Nebraska-Lincoln Department of Chemical and Biomolecular Engineering 820 N 16th St, Lincoln, NE 68588			5e. TASK NUMBER		
			5f. WORK UNIT NUMBER		
8. PERFORMING ORGANIZATION REPORT NUMBER			9. SPONSORING/MONITORING AGENCY NAME(S) AND ADDRESS(ES) Bureau of Reclamation U.S. Department of the Interior Denver Federal Center PO Box 25007, Denver, CO 80225-0007		
10. SPONSOR/MONITOR'S ACRONYM(S) Reclamation			11. SPONSOR/MONITOR'S REPORT NUMBER(S) DWPR Report No. 232		
12. DISTRIBUTION/AVAILABILITY STATEMENT Available from the National Technical Information Service, Operations Division, 5285 Port Royal Road, Springfield VA 22161					
13. SUPPLEMENTARY NOTES Online at https://www.usbr.gov/research/dwpr/DWPR_Reports.html					
14. ABSTRACT A model-guided approach is developed to design and fabricate solar-integrated hollow fiber membrane systems. A multiphysics model was utilized to predict and optimize the performance of hollow fiber membrane modules regarding their water production and energy efficiency. We fabricated membranes with the desired structural parameters and tested them under direct contact membrane distillation (DCMD) operation modes. The experimental results validated the modeling predictions.					
15. SUBJECT TERMS Hollow fiber membrane, module packing, modeling and simulation, solar integration, water desalination, membrane distillation					
16. SECURITY CLASSIFICATION OF:		17. LIMITATION OF ABSTRACT	18. NUMBER OF PAGES	19a. NAME OF RESPONSIBLE PERSON Andrew Tiffenbach	
a. REPORT U	b. ABSTRACT U			THIS PAGE U	19b. TELEPHONE NUMBER (Include area code) (303) 445-2393

**Desalination and Water Purification Research
and Development Program Report No. 232**

Model-Guided Optimal Design and Fabrication of an Integrated Solar- Driven Hollow Fiber Membrane Distillation Module

**Prepared for the Bureau of Reclamation Under Agreement No.
R17AC00139**

by

Dr. Siamak Nejati

Dr. Mona Bavarian

Department of Chemical and Biomolecular Engineering

The University of Nebraska-Lincoln

**U.S. Department of the Interior
Bureau of Reclamation
Technical Service Center
Denver, Colorado**

August 2021

Mission Statements

The U.S. Department of the Interior protects and manages the Nation's natural resources and cultural heritage; provides scientific and other information about those resources; and honors its trust responsibilities or special commitments to American Indians, Alaska Natives, and affiliated Island Communities.

The mission of the Bureau of Reclamation is to manage, develop, and protect water and related resources in an environmentally and economically sound manner in the interest of the American public.

Acknowledgments

The authors would like to acknowledge the financial support from the Bureau of Reclamation, U.S. Department of Interior, through DWPR Agreement R17AC00139. The research was performed, in part, in the Nebraska Nanoscale Facility, National Nanotechnology Coordinated Infrastructure, and the Nebraska Center for Materials and Nanoscience, which are supported by the National Science Foundation under award ECCS 1542182 and the Nebraska Research Initiative.

Acronyms and Abbreviations

Acronym or Abbreviation	Definition
1D	One-Dimensional
2D	Two-Dimensional
3D	Three-Dimensional
CFD	Computational Fluid Dynamics
CPU	Central Processing Unit
DCMD	Direct Contact Membrane Distillation
DMAC	N-N-Dimethylacetamide
DMF	N-N-Dimethylformamide
GB	Gigabyte
HEX	Heat Exchanger
HFM	Hollow Fiber Membrane
iCVD	Initiated Chemical Vapor Deposition
IPA	Isopropyl Alcohol
MD	Membrane Distillation
NMP	N-Methyl-2-Pyrrolidone
NREL	National Renewable Energy Laboratory
PPFDA	Poly (Perfluorodecyl Acrylate)
PTFE	Poly (Tetrafluoroethylene)
PVDF	Polyvinylidene Fluoride
RAM	Random Access Memory
RO	Reverse Osmosis
SDS	Sodium Dodecyl Sulfate
SEC	Specific Energy Consumption
SEM	Scanning Electron Microscopy
SGMD	Sweeping Gas Membrane Distillation
TEP	Triethyl Phosphate

Measurements

Acronym or Abbreviation	Definition
°C	degree Celsius
°F	degree Fahrenheit
cm	centimeter
K	Kelvin
kPa	kilopascal
kWh/m ³	kilowatt-hour per cubic meter
L	liter
Lm ⁻² h ⁻¹	liter per square meter per hour
m	meter
m ²	square meter
m ² /m ³	square meter per cubic meter
mg/L	milligram per liter
mL min ⁻¹	milliliter per minute
ppb	part per billion
ppm	part per million
µg/L	microgram per liter

Nomenclature

Symbol or Abbreviation	Definition
γ	Activity coefficient of water
δ	Membrane thickness (m)
ϵ	Membrane porosity
θ	Temperature polarization
μ	Dynamics viscosity (Pa.s)
Π	Osmotic pressure (Pa)
ρ	Density (kg m ⁻³)
τ	Tortuosity
χ_a	Physical properties of air

Symbol or Abbreviation	Definition
χ_m	Physical properties of the membrane
χ_p	Physical properties of polymer
a	Center to center distance of fibers (m)
B_0	Membrane permeability
C_p	Specific heat capacity of water ($J mol^{-1}K^{-1}$)
c_w	Concentration of water vapor in air ($mol m^{-3}$)
d_p	Pore diameter (m)
D_{eff}	Effective diffusion coefficient ($m^2 s^{-1}$)
D_H	Hydraulic diameter (m)
$D_{n,m}$	Knudsen diffusion coefficient ($m^2 s^{-1}$)
D_t	Total mass diffusion coefficient ($m^2 s^{-1}$)
D_{wa}	Molecular diffusion coefficient of water in air ($m^2 s^{-1}$)
h	Heat transfer coefficient ($W m^{-2} K^{-1}$)
ΔH_{vap}	Heat of evaporation ($J mol^{-1}$)
J_w	Permeate flux ($mol m^{-2} s^{-1}$)
k	Water thermal conductivity ($W m^{-1} K^{-1}$)
k_a	Air thermal conductivity ($W m^{-1} K^{-1}$)
k_m	Thermal conductivity of the membrane ($W m^{-1} K^{-1}$)
\dot{S}_{gen}	Specific entropy generation ($kJ kg^{-1} K^{-1}$)
s	Entropy ($kJ K^{-1}$)
k_p	Polymer thermal conductivity ($W m^{-1} K^{-1}$)
L	Fiber length (m)
M_a	Air molecular weight ($g mol^{-1}$)
M_w	Water molecular weight ($g mol^{-1}$)
\bar{N}_w	Average molar flux of water ($mol s^{-1}$)
Nu	Nusselt number
P_t	Total pressure of the system (Pa)
p	Pressure (Pa)
p_w^{sat}	Vapor pressure of water (Pa)
q	Heat of conduction ($W m^{-2}$)
R_o	Hollow fiber outer diameter (m)
R_i	Hollow fiber inner diameter (m)
Re	Reynolds number

Symbol or Abbreviation	Definition
R	Gas constant ($\text{J mol}^{-1}\text{K}^{-1}$)
Sh	Sherwood number
T_a	Bulk temperature of air (K)
$T_{a,in}$	Air temperature at the inlet (K)
$T_{f,bulk}$	Bulk temperature of feed (K)
$T_{f,in}$	Temperature of feed at the inlet (K)
$T_{a,bulk}$	Bulk temperature of air (K)
$T_{d,bulk}$	Bulk temperature of distillate (K)
T_m	Membrane temperature (K)
$T_{m,l}$	Membrane surface temperature, the lumen (K)
\vec{u}	Velocity vector
v_m	Molar volume of water (m^3)
x_w	Molar fraction of water vapor
X_{NaCl}	Molar fraction of NaCl
\dot{Q}	Specific heat (kJ kg^{-1})
\dot{m}	Flowrate (kg s^{-1})

Table of Contents

Acronyms and Abbreviations	i
Measurements	ii
Nomenclature	ii
Executive Summary	xi
1. Introduction	1
1.1. Project Background	1
1.2. Mathematical Modeling of Membrane Distillation	2
1.3. Solar Water Heater	3
1.4. System Integration.....	4
1.5. Membranes and Materials.....	5
1.6. Project Objectives.....	6
2. Technical Approach and Scope of Work	6
3. Results and Discussion	14
3.1. Effect of Design Parameters on MD Performance: Modeling Studies.....	14
3.1.1. Effect of Packing Configuration on Module Performance	14
3.1.2. Effect of Fiber Interspacing Parameter	16
3.1.3. Effect of Membrane Thickness.....	17
3.1.4. Determining Membrane Diameter for the MD Module.....	18
3.1.5. Effect of Feed and Distillate Velocities.....	19
3.1.6. Comparison of the Efficiency of Direct Contact Membrane Distillation (DCMD) with that of Sweeping Gas Membrane Distillation (SGMD).....	20
3.1.7. Design Optimization for Solar-Driven Hollow Fiber Modules	22
3.2. Model Validation and Fabrication of Prototype HFM Modules	24
3.2.1. Fabricating Hollow Fiber Membranes.....	25
3.2.2. Spacer Fabrication and Assembly.....	26
3.3. Characterization of the Fabricated Modules under Various Operation Modes.....	27
4. Conclusion	31
4.1. Outcomes	31
4.2. Recommended next steps	31
References	32
Metric Conversions	39

List of Figures

Figure 1. Integrated research strategy.....	4
Figure 2. The HFM within its control volume. The locations, directions, and compositions of the feed and distillate can vary.	7
Figure 3. Schematic of the computational unit cell for (a) hexagonal, (b) square, and (c) triangle (close-packed) lattice geometries. Dashed lines and shaded regions are the locations of symmetry planes and computational domains, respectively. Figure 3(d) shows a sample of mesh grids for the triangle (close-packed) computational domain. Here, a , t , and R are the center-to-center distances between neighboring fibers, thickness, and outer radius of the HFM, respectively.	8
Figure 4. The schematic of our strategy involving mathematical modeling and simulation, synthesis, and characterization. The computational/theoretical task provides feedback to the experimental tasks (link A) and the experimental tasks to the computational/theoretical task (link B).	9
Figure 5. Process flow diagram of solar-assisted DCMD with heat recovery	10
Figure 6. Schematic of the dry-jet wet spinning method for the fabrication of HFMs.....	11
Figure 7. Illustration of different steps for the fabrication of HFM modules with organized packing: (a) top and side views of 3D spacers fabricated through additive manufacturing method (3D printing); (b1) passing HFMs through the 3D printed spacers and sealing one end with epoxy; (b2) sliding the other spacer away; (b3) inserting the spacers and HFM bundle into a polycarbonate tube with an inner diameter of 9.525 mm and sealing both ends with epoxy; and (b4) an image of the final version of the assembled module with organized packing.	12
Figure 8. Initiated chemical vapor deposition (iCVD) scheme used to modify the surface of HFMs: (a) schematic of iCVD process; (b) schematic of the reentrant structures created through iCVD, PTFE, and a conformal layer of PPFDA on the surface of the HFM deposited from vapor phase; and (c) image of our iCVD setup	13
Figure 9. Schematic diagram of the laboratory-scale DCMD experimental setup	14
Figure 10. Effect of packing configuration on the normalized permeate flux for HFMs with different lengths: (a) the water vapor flux is normalized to the packing volume; and (b) the water vapor flux is normalized to the membrane area. Here, (Δ), (\square), and (\circ) symbols represent close-packed, square, and hexagonal unit cells, respectively. The membrane outer and inner radii were kept constant at 400 and 300 μm , respectively; the interspacing parameter, R/a , was set to 0.45. The feed and distillate inlet temperatures are 17°C and 80°C, respectively. The fiber porosity and tortuosity are set at 74% and 2.5, respectively.....	15

Figure 11. Effect of the interspacing parameter on the permeate flux: (a) the normalized permeate flux for membranes with various thicknesses; and (b) higher resolution data for a 50 μm thick membrane. Here, the outer radius of the membrane was kept constant at 400 μm . The feed and distillate inlet temperatures were 80°C and 17°C, respectively. The fiber porosity and tortuosity were set at 74% and 2.5, respectively. The length of the fibers was set to 4.5 cm. The shaded area, so-called turning point locus, represents the R/a values beyond which the flux declines rapidly. 17

Figure 12. The effect of membrane thickness on performance. The effect of membrane thickness on the distillate flux and temperature difference across the membrane is shown in (a), and the ratio of conductive and convective heat transfer resistances to the total heat transfer resistance is shown in (b). The hollow fiber outer radius was kept constant at 400 μm . The feed and distillate inlet temperatures were 17°C and 80°C, respectively. The fiber length, porosity, and tortuosity were set at 4.5 cm, 74%, and 2.5, respectively..... 18

Figure 13. The effect of fiber inner diameter on the performance of packing. The effect of fiber inner diameter on the permeate flux, normalized by volume and pressure drop of the module, is shown in (a), and (b) shows the total pressure drop of the module (L=4.5 cm). The ratio of external to internal radii of HFMs was kept constant at 1.33. Here, the velocity of feed and permeate were 1.6 m/s and 0.8 m/s, respectively. The feed and distillate inlet temperatures also were 17°C and 80°C, respectively. The interspacing parameter, fiber porosity, and tortuosity were set at 0.45, 74%, and 2.5, respectively. The shaded area represents the effective range of the inner diameter of HFMs..... 19

Figure 14. The effect of (a) feed stream velocity, and (b) distillate stream velocity on the normalized permeate flux. The membrane outer and inner radii were kept constant at 400 μm and 300 μm . The feed and distillate inlet temperatures were 17°C and 80°C, respectively. The fiber length, porosity, and tortuosity were set at 4.5 cm, 74%, and 2.5, respectively. Here, the inter-spacing parameter is 0.45..... 20

Figure 15. Comparison of DCMD and SGMD results: (a) the change in flux with fiber-to-fiber spacing (interspacing) distance; (b) the changes in the thermal efficiency of the module with fiber interspacing; (c) the variation of the permeate flux and thermal efficiency with the feed temperature; and (d) the effect of HFM thickness on permeate flux. In Figures 15a-c, the membrane thickness was assumed to be 100 μm ; the feed and distillate velocities were 0.08 m/s and 0.8 m/s, respectively. 21

Figure 16. The effect of module length on the flux and specific entropy generation of DCMD module. The flux was obtained from COMSOL and specific entropy generation was calculated using Equations A8 and A17. The simulation was performed for feed and distillate temperatures of 80 °C and 20°C, respectively..... 22

Figure 17. The relative contribution of each entropy generation source to the total entropy generation of solar MD system. The total specific entropy generation is 2871.2 J kg⁻¹ K⁻¹ and

the corresponding second law efficiency is 12.92 percent. Calculations were performed using analyses in Appendix C..... 23

Figure 18. The global irradiance on a flat surface and the corresponding DCMD flux in a typical day: (a) summer day; and (b) winter day. Metrological data were obtained from the NREL National Solar Radiation Database. The simulated results were taken for July 24 and January 17, 2017. 23

Figure 19. A comparison between experimental and computational results. The comparison was done regarding the distillate flux of two HFMs, the prediction of the model at comparable porosities (74% and 68%), and a range of tortuosity factor (τ) for the membranes in a close-packed configuration. The membrane structure, properties, and all parameters describing the geometry and operating conditions are taken from Wang et al (2008). Results shown in (a) represent high porosity and low tortuosity membrane; results shown in (b) represent lower porosity and higher tortuosity membranes. Here, feed velocity is 1.6 m/s; distillate velocity is 0.8 m/s; fiber length, inner diameter, and outer diameter are 20 cm, 600 μm , and 800 μm , respectively. The distillate temperature and fiber inter-spacing parameters are 17°C and 0.45, respectively. 24

Figure 20. Cross-section and top-down SEM images of HFMs..... 25

Figure 21. Cross-section SEM images of modified HFMs. Reentrant structures are created to reduce the surface energy by deposition of particulate structures of PTFE and a conformal layer of PPFDA on the surface of the HFM. 25

Figure 22. Top-down SEM image of (a) pristine and (b) coated HFM. Scale bars in (a) and (b) are 4 and 5 μm . The plot in (c) shows pore size distribution using image analysis on (a) and (b). The mean pore sizes for the pristine and coated HFM were 0.11 and 0.077 μm , respectively. 26

Figure 23. Gas permeation of the pristine and coated HFM. The correlation factors, R^2 , for the pristine and coated HFM were 0.9966 and 0.9972, respectively. 26

Figure 24. Assembling steps of a module consisting of more than 120 number of HFMs: (a) the 3D printed spacers with two rubber O-rings; (b) the 3D-printed spacer after making the organized packing configuration; (c) an assembled version of HFM bundle; and (d) a complete example of the prototype. The packing density of the shown bundle is 3600 m^2/m^3 27

Figure 25. Membrane distillation results of samples including oil contamination. The photograph in (a) shows water samples of 500 ppm, 100 ppm oil, and pure water. Optical microscopic images of 500 ppm oil emulsion and 100 ppm oil emulsion are shown in (b) and (c), respectively. The insets in (b) and (c) display the size of oil droplets using image analysis on the micrographs. Normalized water flux and salt rejection of the pristine membrane ($\phi=9.3\%$) and the coated membrane ($\phi=9.3\%$) are shown in (d), varying concentration of SDS in the feed, in (e) for 100 ppm oil, and in (f) for 500 ppm oil. The feed and distillate temperatures were set to 50°C and 19°C, respectively. The flow rate of feed and distillate was

set to 0.4 L min^{-1} . J_0 of the pristine and coated membranes were (d) 14.3 and $9.25 \text{ L m}^{-2} \text{ h}^{-1}$, (e) 14.5 and $9.5 \text{ L m}^{-2} \text{ h}^{-1}$, and (f) 10.25 and $8.15 \text{ L m}^{-2} \text{ h}^{-1}$, respectively. 28

Figure 26. SEM images of outer surfaces of membranes for (a) pristine and (b) functionalized HFM after accelerated salt scaling experiment. The salt crystals on membranes are circled with a red line. 29

Figure 27. The effect of feed temperature on the water production rate per volume of modules with different packing densities. 30

Figure 28. Comparison of experimental and simulations results. The plot in (a) shows the effect of feed temperature on the permeation flux. Here, the packing density of the module was $250 \text{ m}^2/\text{m}^3$, and feed and distillate velocities were set at 0.01 and 0.8 m/s , respectively. The plot in (b) shows the effect of feed velocity on the permeate flux. Here, the feed temperature was set at 40°C 30

List of Tables

Table 1. Operating conditions used to perform the DCMD simulations..... 8

Table 2. Spinning conditions of HFMs..... 11

This page intentionally left blank.

Executive Summary

To date, membrane distillation (MD) has not been commercialized as a viable technology for water desalination, mainly due to its high specific energy consumption when compared with that of other membrane-based processes, such as reverse osmosis (RO). However, the possibility of operating MD on low-grade heat sources provides an opportunity to develop MD-based desalination schemes with a reduced energy footprint. In this study, we developed an integrated solar-driven MD process based on high packing density hollow fiber membrane (HFM) modules. An 18-month effort was dedicated to developing a hybrid mathematical and experimental approach for the design and fabrication of optimized membrane modules with an enhanced water production rate.

High-performance modules were fabricated; these modules had a normalized water production rate of $35 \pm 5 \text{ Lm}^{-2}\text{h}^{-1}$ when the feed and distillate temperatures were kept at 70°C and 20°C , respectively. To configure a membrane module and a standalone solar-driven MD system, we determined the optimal geometrical parameters and operating conditions using a first-principles mathematical model and then validated our design experimentally.

For the HFM module, we investigated the effect of various parameters on the module performance, such as fiber-fiber interspacing, the physical properties of the fibers, and the feed temperature and concentration. Relying on state-of-the-art technologies, such as chemical vapor deposition and three-dimensional manufacturing, we developed robust laboratory-scale modules. Our calculations suggest that the developed prototypes can be coupled with commercially available flat plate solar collectors and desalinate water with an estimated specific energy consumption of 10 kWh/m^3 . To further enhance the robustness of our modules, we used our novel initiated chemical vapor deposition (iCVD) process and assembled omniphobic structures on the surface of these membranes. The application of omniphobic coatings resulted in about an 86 percent reduction in salt scaling. In addition, we devised chemical processes for the functionalization of HFMs so that water resources contaminated with oil could be processed in MD. Then, depending on the composition of the feed, we developed methodologies for increasing water recovery using MD. Our analyses indicate that for approximately 150 fibers packed in a module with a packing density around $3,600 \text{ m}^2/\text{m}^3$, about 50 liters of deionized water can be collected each day using solar energy for heating the saline water.

This page intentionally left blank.

1. Introduction

1.1. Project Background

Brackish groundwater – defined as water with a total dissolved solids concentration in the range of 500-35,000 mg/L – is one of primary source of water for many inland and coastal communities. Currently, a significant portion of groundwater is being used for irrigation, but it is expected that groundwater will become a substantial source for almost 40 percent of public water supplies across the United States by 2050 (Maupin et al. 2014). This number is projected to increase as a result of climate change and growing demand (Roy et al. 2012). Thus, emerging desalination technologies, enabling the treatment of brackish groundwater, will become more attractive for both research and real-world applications. Among different techniques, membrane-based water desalination is one of the most sustainable methods to produce drinking water. Membrane distillation (MD), a thermally driven membrane-based separation process, is among the potential candidates for the treatment of saline and brackish water. The theoretical, non-selective, 100 percent rejection value for the non-volatile species – a unique feature of the MD process – makes MD suitable for removing solutes and ions (Hou et al. 2010; Qu et al. 2009; Yarlagadda et al. 2011). Today, most desalination technologies rely on fossil fuel resources for providing the required energy for pumping fluids, heating, and cooling (Kavvadias and Khamis 2014; Ghaffour et al. 2013; Qtaishat and Banat 2013; Shatat et al. 2013). To reach a fully sustainable solution and to reduce the environmental impact associated with the use of fossil fuels as the energy resource, the optimal coupling of desalination technology with renewable and pollution-free energy resources is of high importance. Among alternative renewable energy resources, solar energy is an attractive choice: solar energy is abundant, and the technologies converting the solar radiation into electrical and thermal energy have already matured and been deployed on the industrial scale (Shatat et al. 2013; Singh 2013; Kalogirou 2004).

Although a promising technology, MD has not been fully commercialized for water desalination, mainly because the numbers for the specific energy consumption for MD-based processes are not attractive. This shortcoming is partly associated with the lack of high-performance MD modules, setting the specific energy consumption (SEC) for the MD-based desalination two orders of magnitude higher than that of reverse osmosis (RO). However, the capability of operating the MD process at low temperatures provides an opportunity to develop novel schemes that allow for reducing the energy footprint of MD. When one can tap into solar energy as the heat source, MD for desalination of brackish water becomes a practical solution for providing potable water in rural/remote inland areas, where the point-of-use approach for small communities is favored, and the operational and maintenance cost of a commercial desalination plant (e.g., RO) is well beyond the resources available to these communities (Ghaffour et al. 2013; Hogan et al. 1991). Additionally, the exceptional rejection values for MD membranes allow for desalinating groundwater supply, even for those situated inland (Gates et al. 2011; Neidhardt et al. 2012; Norra et al. 2005). Considering all the features of MD technology, more

research and development is required to overcome the challenges facing the desalination schemes based on MD, such as the low flux limitation of the modules.

A handful of reports exist on the solar-MD integration from both the conceptual and experimental points of view; however, none of the reported values for the SEC of these integrated technologies is on par with the SEC of an RO system (Chafidz et al. 2016; Kim et al. 2013; Kim et al. 2016). Recently, it has been shown that the MD module has the potential to provide a significantly large flux when the membranes are specifically designed for MD applications (Bonyadi and Chung 2009; Zuo et al. 2016; Nejati et al. 2015).

Additionally, the importance of module design and fabrication has been pointed out by many researchers, and it is still among the active research areas (Koutsou et al. 2015; Mat et al. 2014; Yang et al. 2011). MD modules, based on flat sheet membranes, can be fabricated into plate and frame or more sophisticated designs, such as spiral wound modules. Nonetheless, the highest packing density, 500-9,000 m²/m³, for a module can be achieved using hollow fiber membranes (HFMs) (Souhaimi and Matsuura 2011). Excellent mass transfer coefficient, mechanical strength, and ease of handling during fabrication and operation of the module result from switching from a two-dimensional (2D) flat sheet geometry to a three-dimensional (3D) hollow fiber structure (Feng et al. 2013; Sun et al. 2012).

Apart from the membrane module, the operation scheme is another area for the development of the MD process. Various modes of operation, such as direct contact, air gap, sweeping gas, and vacuum membrane distillation, have been proposed and tested. Direct contact membrane distillation (DCMD) is the most frequently used method for MD operation. Sweeping gas membrane distillation (SGMD) is now gaining more attention because of its favorable energetics (Amy et al. 2017; Khayet et al. 2003b; Karanikola et al. 2015). The relatively lower conductive heat loss through the membrane in the SGMD operation results in a higher driving force for transmembrane mass transport.

Moreover, in this configuration, resistance to the mass transport at the permeate side of the membrane is continuously reduced because of the unceasing removal of water vapor by the gas flow (Karanikola et al. 2017; Tomaszewska 2015). For instance, the comparison of similar membranes under DCMD and SGMD operation showed that the permeate flux in the SGMD process is 40 percent higher than that of DCMD (Khayet et al. 2003a). In SGMD, by using high-efficiency condensers, we can significantly enhance system efficiency (Souhaimi and Matsuura 2011; Alkudhiri et al. 2012). Thus, from a practical viewpoint, there is a need to identify the limiting processes in MD operation by investigating the effects of module characteristics and processing parameters. This effort can enable the realization of MD as a viable and clean technology for the treatment of contaminated water – especially in remote inland areas with no access to seawater and where the cost of water production is higher.

1.2. Mathematical Modeling of Membrane Distillation

Mathematical modeling has been widely used to fully understand the effect of the parameters determining the water flux of an MD module (Lian et al. 2016; Upadhyaya et al. 2016). A

multiphysics modeling approach helps to understand the impact of flux-determining factors in a module. In MD, due to the difference in water vapor pressure between the feed and distillate streams, water vapor diffuses through the membrane and reaches the other side. The rate of transport from the feed side to the permeate side is strongly dependent on the temperature difference, the pressure of the system, and membrane properties (e.g., porosity, tortuosity, and length). Therefore, it is necessary to solve a system of coupled mass, momentum, and energy equations to predict system performance.

Typically, the most straightforward simulation methodology is to reduce the model to one dimension (1D). This method is very efficient for treating a membrane in flat sheet geometry; however, it does not provide an accurate picture for a hollow fiber module under operation. This approach not only disregards the variations in pressure and temperature of flow streams through the module length but also neglects the effect of module configurations on transport properties. Thus, several efforts have been devoted to model the process in 2D space to consider the effect of pressure and temperature changes along the module (Marcos et al. 2009; Sohrabi et al. 2011; Azari et al. 2016; Marjani et al. 2016; Yan et al. 2014).

However, a 2D approach fails to consider the impact of different module configurations, which is one of the most important factors influencing the water production rate and energy efficiency of the HFM module. Hence, to capture the full picture of HFM modules under operation, a 3D model is needed. A 3D model allows us to study the effect of packing geometry and on distillate flow and can be adapted to predict the impact of module configuration on the water production rate.

1.3. Solar Water Heater

Solar collectors are classified according to their motion, i.e., stationary, single-axis tracking, and two axes tracking, and to the temperature that can be reached by the thermal fluid in the collectors (Qtaishat and Banat 2013; Banat et al. 2002). Among various designs, flat-plate and evacuated tube collectors have been widely used in the laboratory and pilot-scale systems for integration with the MD system (Ding et al. 2005).

The instantaneous efficiency of a solar thermal collector is defined as the ratio between the useful energy delivered, Q (W), over aperture area, A (m^2), and the insulation, I (W/m^2), which is incident on the aperture:

$$\eta = Q/AI \quad (1)$$

In the last three decades, extensive research has been done to model the flat plate solar collector's performance (Wang and Wu 1990). Oliva et al. developed a multidimensional model of the solar collector components including glass cover, tubes, and insulation (Oliva et al. 1991). Selmi et al. simulated a flat-plate solar collector by using the commercial CFD software CFD-ACE+® (Selmi et al. 2008). The numerical results agreed well with the experimental temperature profile. By breaking this system into the constituent subsystems, including the cover, the air gap between the cover and the absorber, fluid flow, absorber, and the insulation layer, Villar et al.

presented a 3D numerical model for the flat-plate solar collector (Villar et al. 2009). Thus, the effect of the non-uniform flow and temperature distribution on collector efficiency was investigated. These models can represent the thermal performance of the solar collector in the presence of variation in solar radiation (Villar et al. 2009). Therefore, the daily energy yield and variations in the water temperature can be predicted in a transient mode. These models can be easily integrated with the model for the HFM modules to predict the performance of a solar-integrated HFM using first-principles mathematical modeling.

1.4. System Integration

In the last decade, the coupling of membrane distillation modules with solar energy collectors has been investigated by many researchers. Banat et al. studied the production of potable water from seawater by integrating an MD module with a solar still (Banat et al. 2002). Ding et al. developed a mathematical model of the solar-driven MD system to produce pure water from brackish water (Ding et al. 2005). Koschikowski et al. conducted experimental studies to investigate the production of potable water from brackish and seawater using a solar thermal-driven spiral-wound PTFE MD module (Koschikowski et al. 2003). Despite these efforts, we still lack the first-principles mathematical models that can adequately describe a solar-driven hollow fiber MD module (Koschikowski et al. 2003). In our project, we developed a detailed first-principles transient model of a hollow fiber MD module. The developed model was used to evaluate performance over all the hollow fiber MD module design parameters. We systematically searched for and arrived at the design specifications of optimal materials and optimized the module operation and integration. In this project, we used a model-guided strategy, shown in Figure 1, to address the critical needs in the current status of solar-driven hollow-fiber MD modules.

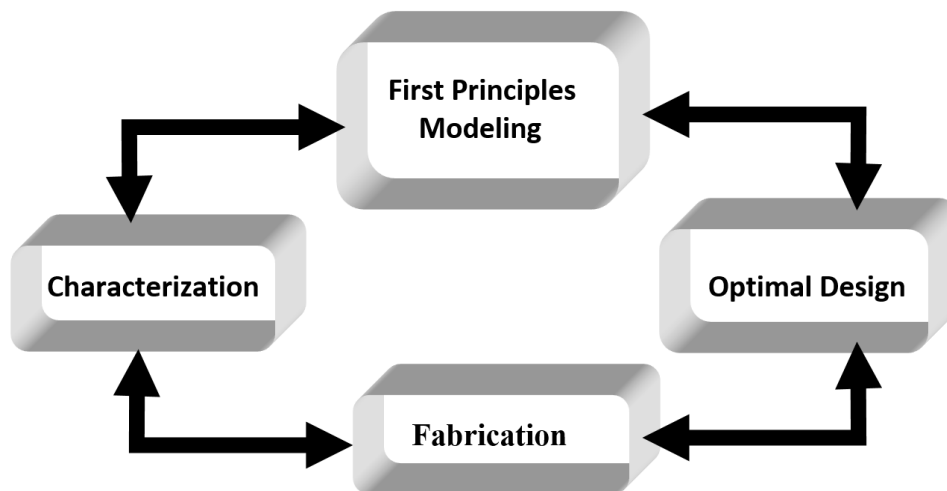


Figure 1. Integrated research strategy

The energy and cost analyses in thermal distillation and membrane desalination processes such as RO are well known and described; however, only a few studies have been done to analyze

energy consumption for the MD process. It has been reported that thermal efficiency is very sensitive to the feed temperature (Khayet 2013). This has been attributed to the exponentially increased mass flux and to the reduction of the amount of heat lost by conduction through the membrane with the increase of the feed temperature. To develop and formulate an energy consumption model, we considered the energy required for the MD process and all the processing equipment, including pumps and/or compressors, which is dependent on membrane configuration and operational condition.

1.5. Membranes and Materials

HFM in MD modules are made of hydrophobic materials. In general, hydrophobicity is a requirement for MD membranes. Hydrophobic, superhydrophobic, and omniphobic materials are all proposed to be utilized as MD membrane materials. The rationale behind these choices is to avoid wetting and fouling during MD operation (Boo et al. 2016; Lin et al. 2014; Servi et al. 2016). In the past two decades, significant breakthroughs in the development of surfaces with special wettability have been achieved and guidelines for creating well-defined curvature and topographies have been reported (Tuteja et al. 2007; Tuteja et al. 2008). Nonetheless, this knowledge was not employed for membrane fabrication until very recently (Lin et al. 2014; Ma et al. 2016). Few commercial membranes possess self-cleaning properties suitable for use in MD processes. This shortcoming could be mainly due to the complexity and the cost associated with the fabrication process and materials. Current activities in the development of omniphobic membranes are promising, and novel approaches and methods have been applied to create such matrices. One of the main challenges is the heavy reliance on silanization, i.e., grafting silane compounds to the surfaces, as an essential step in adjusting the surface wettability (Boo et al. 2016; Lin et al. 2014; Lee et al. 2016; Paxson et al. 2014). Additionally, creating re-entrant structures (containing domains with both positive and negative curvatures) on the membrane surface has been a significant challenge, and the schemes and methods developed to date often rely on cumbersome post-processing methods.

Currently, HFM is being mass-produced and many methods for packing of the membrane have been introduced (Mat et al. 2014). The development in the fabrication of HFMs for MD has been relatively slow, mainly due to the lack of a vast library of chemicals that are hydrophobic and solvent tractable. Additionally, the use of phase inversion to fabricate membranes is an art rather than a science, and the governing phenomena driving the process are not entirely understood. Thermodynamic parameters such as Flory-Huggins interaction parameters in the polymer mixture equation of state are often estimated, and no direct measurement exists for evaluating the effect of these parameters on the phase inversion process. Efforts to simulate phase inversion have been only marginally successful (Zhu et al. 2016). The experimental space for parameters influencing the phase inversion process is limitless, and as a result, the use of different compositions for dope solutions, additives, solvent-non-solvent choice, etc., can drastically change the process trajectory, controlling the resulting final structure of the membranes. It is expected that in the near future, with the help of the black-box modeling and machine learning approach, we will be able to navigate the space of membrane fabrication and

converge at a variety of formulations that can be used for membrane fabrication (Haase et al. 2015).

Membrane surface and interfacial domains in the separation process is another key parameter in membrane-based separation. As mentioned, fluoropolymers are among the most used materials in MD. Our ability to control the surface of MD membranes, unlike with other membrane surfaces, has been slow to develop. This is due to the chemical stability of fluoropolymers, making the chemical adjustment of the surface a challenging task. In the past two decades, an advanced and scalable technology, initiated chemical vapor deposition (iCVD), has been demonstrated as a useful all-dry technique for the synthesis of polymer thin films and coatings (Coclite 2013). By adjusting iCVD parameters, thin films of fluoropolymer can be deposited on various substrates. It has been shown that this approach is efficient in applying thin films over complex topography, creating stable and highly hydrophobic surfaces (Lau et al. 2003). This method provides an opportunity to render various substrates superhydrophobic through a straightforward and scalable approach (Ghaleni et al. 2019; Gleason 2019); as a result, its application in designing materials for MD is expected to grow.

1.6. Project Objectives

The ultimate objective of this work was to develop a hybrid mathematical and experimental approach for identifying the critical parameters limiting the application of HFM modules for the desalination of brine. Gaining an understanding of the effect of the design and configuration of the membrane module and conducting system-level simulations of a stand-alone solar-driven MD system were among the high-level objectives of the project. A comprehensive approach was taken where first-principles in a 3D mathematical model provided a detailed understanding of mass transfer in the module, which then efficiently guided the design and fabrication of fibers and modules. This approach led to the design of a new MD module – the fabrication of an optimized hollow-fiber MD system with significantly higher flux above the state-of-the-art hollow fiber MD modules ($35\text{-}40 \text{ Lm}^{-2}\text{h}^{-1}$).

2. Technical Approach and Scope of Work

The proposed research was pursued via four main tasks as outlined below.

- Task 1. Development of detailed macroscopic first-principles mathematical model
- Task 2. Design optimization for solar-driven hollow fiber modules
- Task 3. Fabrication of a prototype for HFM module
- Task 4. Characterization of the fabricated module under various modes of operation

Task 1. Development of a detailed macroscopic first-principles mathematical model

To develop a detailed macroscopic first-principles mathematical model for a hollow-fiber MD module, we broke down the system into a few subsystems and then solved the governing equations for momentum, energy, and mass transfer. For the HFM module, we chose a 3D computational domain, considering the symmetrical arrangement for the fibers in the module; see Appendix A for more details. By breaking the system into three sub-systems ((a) feed stream, (b) membrane domain, and (c) permeate stream) for different packing geometry and lattice dimension and configuration, we solved the governing equations predicting the performance of the MD module under operation. Figure 2 shows a schematic of the model we developed for the simulation of a hollow fiber module.

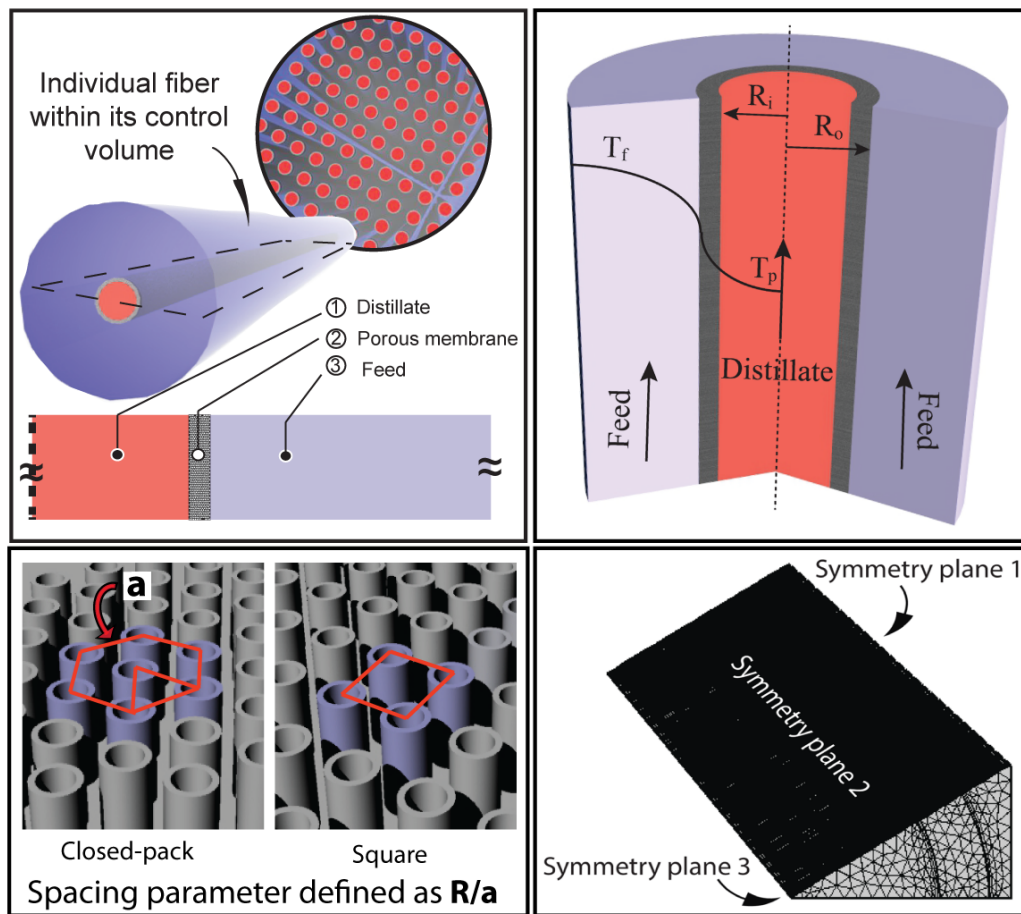


Figure 2. The HFM within its control volume. The locations, directions, and compositions of the feed and distillate can vary.

We solved the coupled mass, momentum, and energy transfer equations, interfaced with MATLAB codes for system-level analysis, using one computing node, including 16 CPU cores (3.2 GHz) and 128 GB RAM. Three packing configurations were considered to study the effect of hollow fiber arrangement on the permeation flux and energy efficiency of the system. For the 3D modeling, the computational domain includes the symmetrical part of an HFM in the control volume of the shell. Figure 3 shows the unit cell of different lattice geometries, where

the shaded regions are the symmetrical computational domain assumed for each configuration. Table 1 presents the range of operating and physical parameters we used in the simulations.

Table 1. Operating conditions used to perform the DCMD simulations

Parameter	Value
Feed temperature (T_f)	303-353 K
Distillate temperature (T_d)	290-300 K
Feed velocity (V_f)	0.2-2 m/s
Distillate velocity (V_d)	0.2-2 m/s
Fiber outer radius (R_o)	50-400 μm
Fiber inner radius (R_i)	40-300 μm
Reynolds number (distillate)	100-1,000
Pore diameter (d_p)	0.2-0.45 μm
Tortuosity (τ)	1.5-8
Porosity (ϵ)	0.68-0.74
Fiber length (L)	4-25 cm
Feed salinity (seawater)	35,000 mg/L
Membrane material	PVDF
Reynolds number (feed)	100-2000

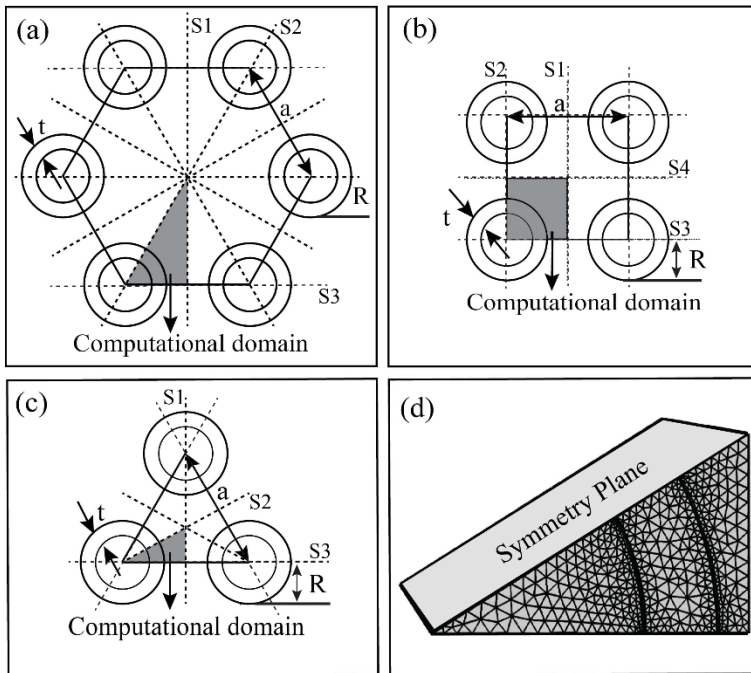


Figure 3. Schematic of the computational unit cell for (a) hexagonal, (b) square, and (c) triangle (close-packed) lattice geometries. Dashed lines and shaded regions are the locations of symmetry planes and computational domains, respectively. Figure 3(d) shows a sample of mesh grids for the

triangle (close-packed) computational domain. Here, a , t , and R are the center-to-center distances between neighboring fibers, thickness, and outer radius of the HFM, respectively.

Task 2. Design optimization for solar-driven hollow fiber modules

Using the developed model for the DCMD in HFM modules with different parameters and configurations, the permeate fluxes were estimated. Figure 4 presents our strategy in modeling and optimization. We conducted our search routine in the space of parameters to find the optimum design and operational conditions for these modules that allow minimizing the SEC. The same strategy was implemented, and a similar model was presented, for the SGMD system; see Appendix A for the detailed DCMD and SGMD models. Using this model, the design and operating conditions that allow for minimizing energy consumption while maximizing the permeate flux were identified. This was done by feeding the optimized flux from the 3D model into a 0D model of a solar-MD process, shown in Figure 5.

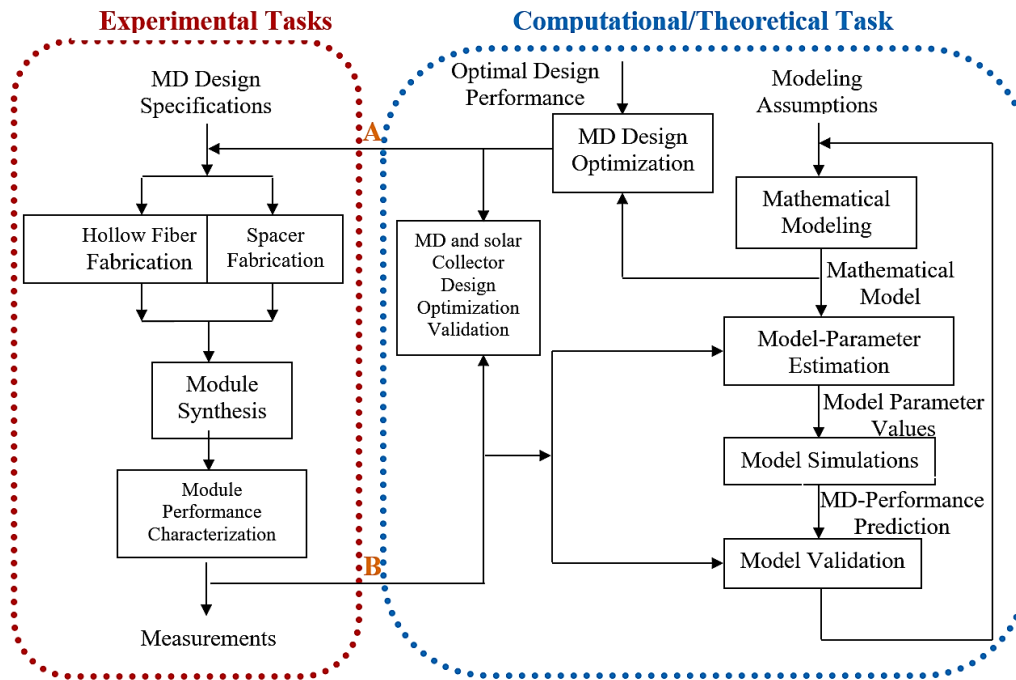


Figure 4. The schematic of our strategy involving mathematical modeling and simulation, synthesis, and characterization. The computational/theoretical task provides feedback to the experimental tasks (link A) and the experimental tasks to the computational/theoretical task (link B).

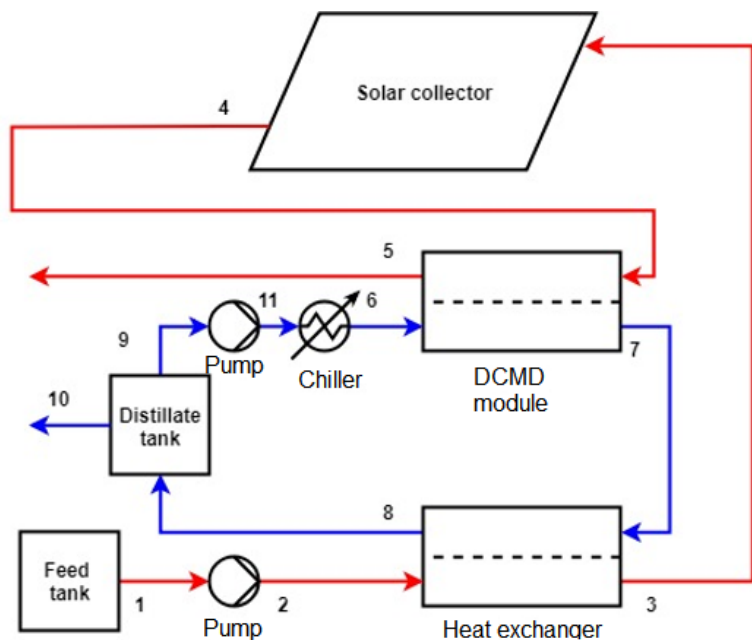


Figure 5. Process flow diagram of solar-assisted DCMD with heat recovery

We conducted the system-level calculation for a variety of operating modes and scenarios with the consideration of the disturbances, such as insulation level, and the results were used to optimize the module's design.

Task 3. Fabrication of a prototype for the hollow fiber membrane module

Subtask 3.1 Fabricating hollow fiber membranes.

To fabricate HFMs, we chose polyvinylidene fluoride (PVDF) and dissolved it in triethyl phosphate (TEP) to make our dope solutions. The HFMs were fabricated using a dry-jet wet spinning method, shown in Figure 6. The dope and bore were fed to the spinneret (DeltaE Srl, Italy) using high-pressure syringe pumps (Fusion 6000, Chemyx, Inc., USA). The nonsolvent-induced phase inversion process occurred in a 1 L graduated cylinder filled with the coagulation bath. The nascent fibers were left in the coagulation bath for 10 minutes and then transferred to a water bath. The water bath was changed after 24 hours and exchanged with isopropyl alcohol (IPA) after 48 hours. The fibers were left in the IPA bath for another 24 hours to remove excess TEP from the fibers. Finally, the HFMs were dried in the vacuum oven at 50°C for 24 hours. Table 2 lists the detailed spinning parameters for membrane fabrication. The parameters were chosen based on a previous study (Chang et al. 2017).

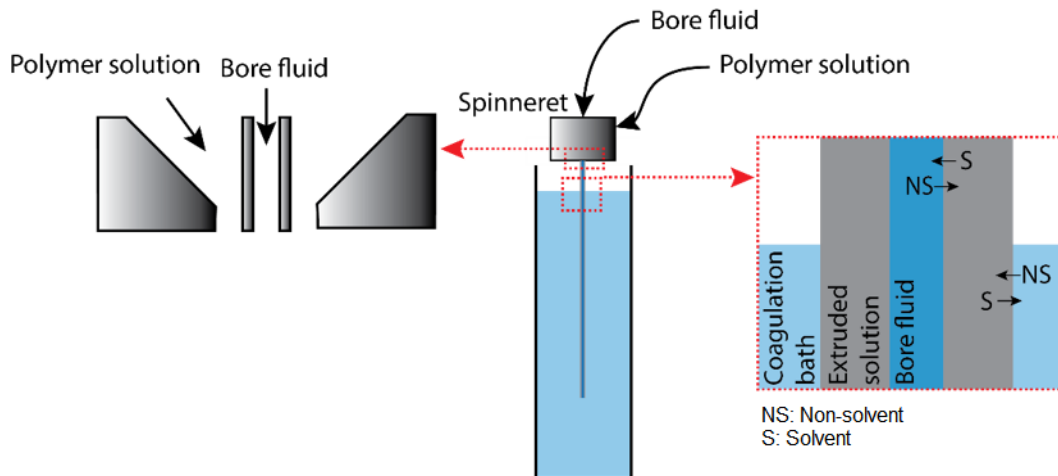


Figure 6. Schematic of the dry-jet wet spinning method for the fabrication of HFMs

Table 2. Spinning conditions of HFMs

Parameter	Value
Dope composition	12 wt.% PVDF/TEP
Dope flow rate	2.5 mL min ⁻¹
Bore composition	20 v/v% TEP/water
Bore flow rate	1.5 mL min ⁻¹
Coagulation bath	30 v/v% TEP/water
Air gap distance	3 cm

Once the membranes were fabricated, they were characterized by both direct and indirect measurements. To obtain structural information, we characterized all the membranes using a Field Emission Scanning Electron Microscope. To obtain cross-section images, membranes were freeze-fractured using liquid nitrogen. The average membrane thickness was determined from the cross-sectional scanning electron microscopy (SEM) images.

Subtask 3.2 Spacer fabrication and assembly

To fabricate spacers, we drew our design using the ANSYS SpaceClaim software from which the CAD files were transferred to the Objet500 Connex3, an advanced multi-material 3D printing system with a precision of 20 μm . Modules' spacers with various R/a ratios, lengths, and dimensions were printed. The designed module spacers include perforated disks, with an exact R/a ratio and a known number of holes for holding the fibers. The fibers were epoxy-glued into the spacers, using a syringe filled with Gorilla epoxy, and the spacer-fiber assembly was enclosed in a polycarbonate casing. The schematic representation of the process used for module fabrication is shown in Figure 7.

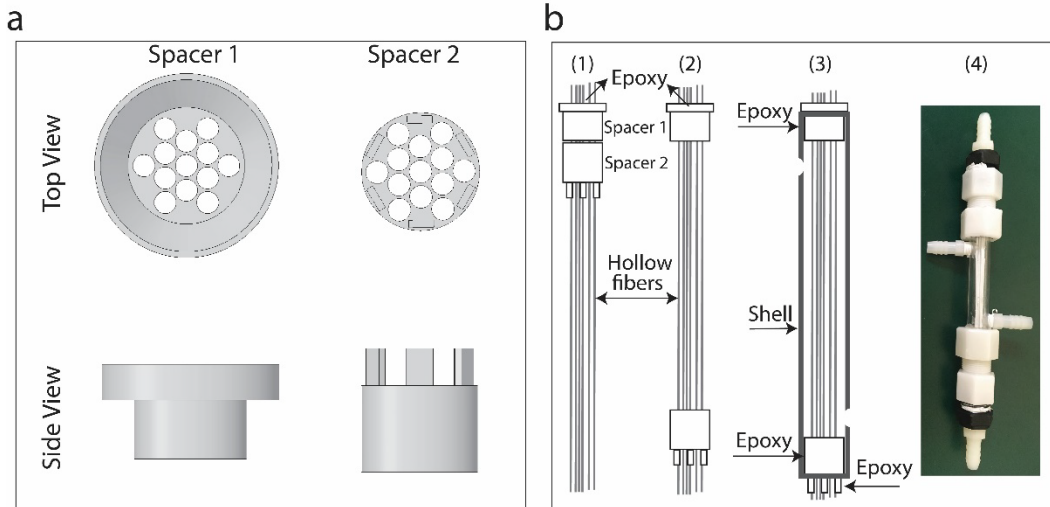


Figure 7. Illustration of different steps for the fabrication of HFM modules with organized packing: (a) top and side views of 3D spacers fabricated through additive manufacturing method (3D printing); (b1) passing HFMs through the 3D printed spacers and sealing one end with epoxy; (b2) sliding the other spacer away; (b3) inserting the spacers and HFM bundle into a polycarbonate tube with an inner diameter of 9.525 mm and sealing both ends with epoxy; and (b4) an image of the final version of the assembled module with organized packing.

Subtask 3.3. Controlling the surface chemistry of membranes

The outer surfaces of HFM were rendered omniphobic through initiated chemical vapor deposition (iCVD); see Appendix C for details on the procedure. iCVD is a unique liquid-free process with the capability of synthesizing polymer thin films with sub-10 nm precision and desired physical properties. During iCVD, as illustrated in Figure 8, the molecules of a radical initiator are thermally cleaved by a filament array kept at 200-300°C. This temperature is only enough to activate the initiator, while the monomer molecules are preserved. The activated initiator radicals react with the monomer on the surface, creating monomer radicals on the surface. The radicals present on the surface provide the anchor points for synthesizing grafted polymer chains. By holding the substrate temperature low (typically, 0-40°C), additional monomer units adsorb on the surface and react with the surface radical, leading to an increased chain length of the grafted polymers. In the iCVD process, the functional groups of monomers are fully retained. This characteristic enables us to have precise control over the physical properties of the deposited films.

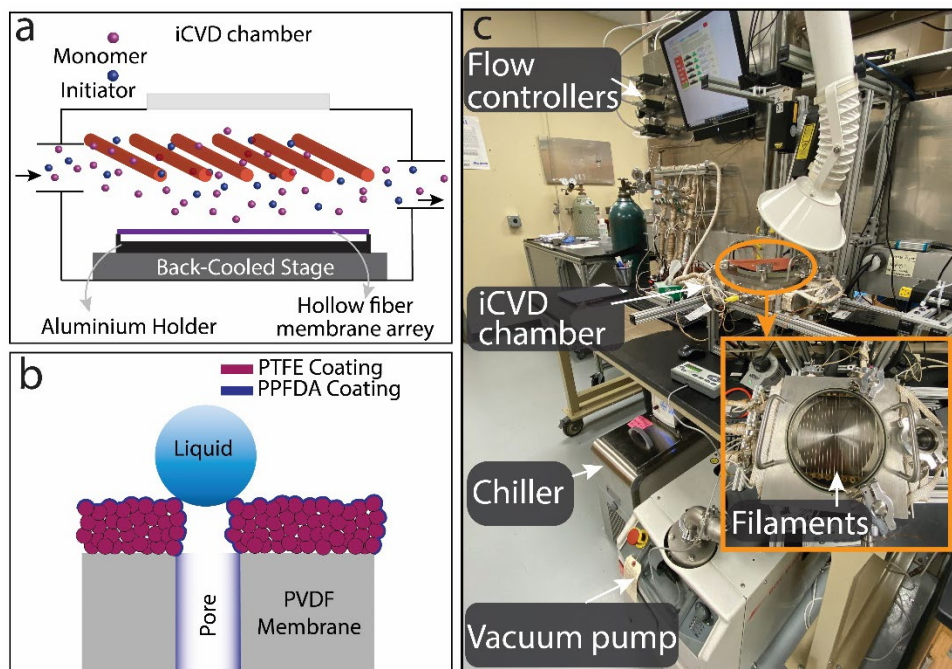


Figure 8. Initiated chemical vapor deposition (iCVD) scheme used to modify the surface of HFMs: (a) schematic of iCVD process; (b) schematic of the reentrant structures created through iCVD, PTFE, and a conformal layer of PPFDA on the surface of the HFM deposited from vapor phase; and (c) image of our iCVD setup

To create polymeric reentrant structures on porous HFM surfaces, we developed a sequential process using our unique iCVD method. Our nanofabrication scheme consists of two steps: (i) building up the reentrant structures, and (ii) adjusting the surface energy. In the first step, we applied a porous film of vertically grown polytetrafluoroethylene (PTFE) polymer to the outer surface of HFMs. Then, we adjusted the surface energy of the assembled PTFE structure by grafting a fluorinated polymer, poly (perfluorodecyl acrylate), PPFDA, to reduce the surface energy. Our iCVD setup used for adjusting surface properties is shown in Figure 8c.

Task 4. Characterization of the fabricated module under various operation modes.

The performance of the fabricated module was evaluated in a laboratory-scale direct contact membrane distillation (DCMD) unit using 1 M NaCl feed solution and DI water distillate stream. Hot feed and cold distillate streams were circulated using two variable gear pumps and the temperatures were kept constant using two recirculating water baths. The feed and distillate circulated at various flow rates and in various modes (counter/co-current). Water vapor flux, J_w , across the membrane was measured by monitoring the increase in distillate mass using a digital balance. The distillate weight was recorded on a laptop at 1-minute intervals. The salt passage was monitored by measuring the salt concentration in distillate using a calibrated conductivity meter at 1-minute intervals. Figure 9 shows the set-up for characterization.

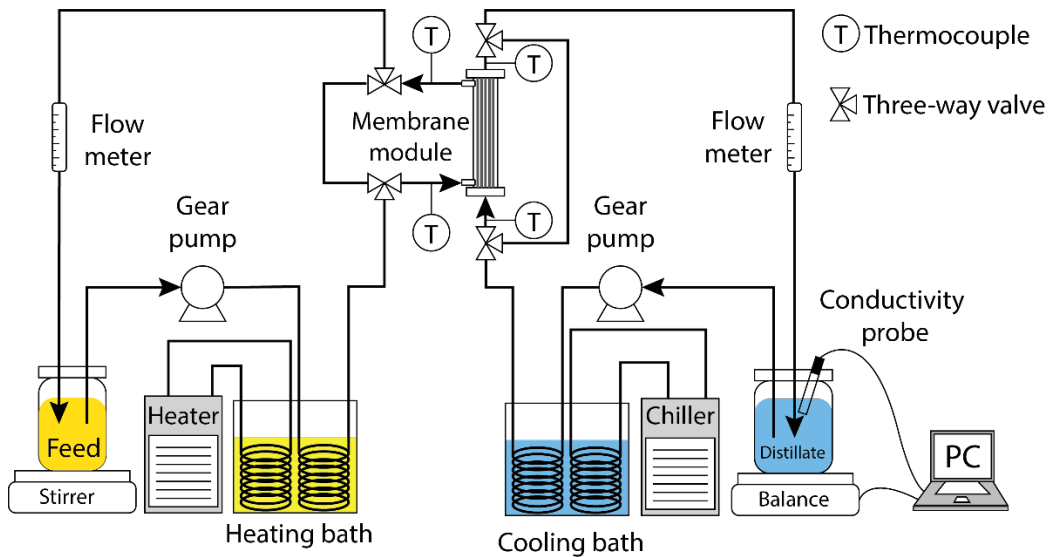


Figure 9. Schematic diagram of the laboratory-scale DCMD experimental setup

3. Results and Discussion

3.1. Effect of Design Parameters on MD Performance: Modeling Studies

3.1.1. Effect of Packing Configuration on Module Performance

Packing configuration is one of the most critical parameters influencing thermal efficiency and permeate flux of the HFM modules used in the MD process. To elucidate the importance of packing geometry on the module performance, three packing configurations – close-packed, square, and hexagonal – were considered. Figure 10 shows the normalized permeate flux for the three packing arrangements. The results indicate that the permeate flux for the close-packed configuration is, on average, 18 percent and 54 percent higher than that of the square and hexagonal configurations, respectively. This enhancement in the flux is expected because the close-packed configuration provides higher packing density compared to the other packing configurations. The close-packed configuration offers 16 percent and 50 percent higher volumetric surface area compared to that of the square and hexagonal configurations, respectively. Hence, the additional enhancement in the flux is expected to correlate directly with the effect of the geometry of the packing on the underlying heat, mass, and momentum transfer in the system. To elucidate the effect of flow pattern and thermal efficiency on the permeate flux, we normalized the permeate flux to the surface area of the membrane. As shown in Figure 10b, the permeate flux for a module with a close-packed fiber arrangement is higher than that of a module with hexagonally packed fibers. The same trend can be observed when comparing the

module with the fibers packed in the square lattice and the close-packed lattice. However, when the module length extends beyond 20 cm, a crossover in the permeate flux can be observed. This crossover can be explained by the effect of module arrangement on the convective heat transfer coefficient and the influence of membrane temperature on the effective diffusion coefficient for the water vapor in the membrane.

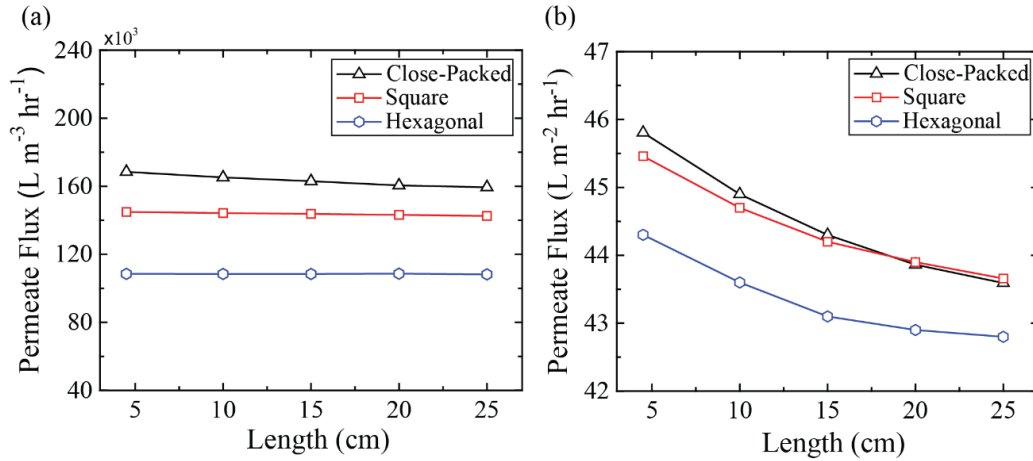


Figure 10. Effect of packing configuration on the normalized permeate flux for HFMs with different lengths: (a) the water vapor flux is normalized to the packing volume; and (b) the water vapor flux is normalized to the membrane area. Here, (Δ), (\square), and (\circ) symbols represent close-packed, square, and hexagonal unit cells, respectively. The membrane outer and inner radii were kept constant at 400 and 300 μm , respectively; the interspacing parameter, R/a , was set to 0.45. The feed and distillate inlet temperatures are 17°C and 80°C, respectively. The fiber porosity and tortuosity are set at 74% and 2.5, respectively.

The effect of packing density on the flow and thermal efficiencies of the module can be explained by calculating the convective heat transfer coefficient and temperature polarization on the feed side. The convective heat transfer coefficient of the close-packed configuration is higher than that of other configurations due to a lower hydraulic diameter in the feed channel of close-packed configuration when compared with the other configurations ($h \propto D_H^{-0.41}$). Our simulations indicate that the area-averaged convective heat transfer coefficients for the close-packed, square, and hexagonal configurations were 5,834 W/m² K, 4,711 W/m² K, and 3,637 W/m² K, respectively. A higher convective heat transfer coefficient at the feed side increases the membrane temperature, leading to a higher diffusion coefficient for the water vapor in the membrane ($D_{w-a} \propto T_m^{2.072}$).

On the other hand, a higher convective heat transfer coefficient will increase the heat loss through the conduction between feed and distillate streams impacting the energy efficiency and transmembrane temperature gradient. The effect of this phenomenon can be seen in Figure 10b, where the area-normalized flux of the square packing configuration becomes slightly higher than that of the close-packed configuration for the module exceeding 20 cm in length. Therefore, a trade-off exists between improving the convective heat transfer coefficient and the energy efficiency of the module.

Another important parameter is the temperature polarization (θ), representing the temperature gradient between the bulk of flow and the membrane's surface. We calculated the temperature polarization of different configurations using the following equation (Khayet and Matsuura 2011):

$$\theta = \frac{T_{mf} - T_{md}}{T_f - T_d} \quad (1)$$

The results showed that the temperature polarization of all configurations remains constant along with the module. The close-packed configuration showed less temperature polarization. The polarization for close-packed, square, and hexagonal configurations (module length=20 cm) was 0.9, 0.86, and 0.85, respectively, where the value of unity is an ideal case. Since the close-packed configuration showed higher permeate flux and thermal efficiency, we chose to use this configuration to further study the effect of various parameters on the performance of the module.

3.1.2. Effect of Fiber Interspacing Parameter

The center-to-center distance between neighboring fibers is another parameter influencing packing density and transport phenomena in the module. If the HFMs are packed in such a way that their outer surfaces are in contact with each other, significant active surface areas in the module will become unavailable. Additionally, this state results in a significant pressure drop and flow misdistribution due to the spatial constriction (Chen and Hlavacek 1994; Zheng et al. 2003; Bao and Lipscomb 2002). On the other hand, if we allow for a large center-to-center distance between fibers, the packing density, convective heat transfer coefficient, and the permeate flux decrease. Therefore, it is essential to find a distance between fibers that provides the highest permeate flux and thermal efficiency.

We defined a dimensionless parameter (interspacing parameter), R/a , the ratio of outer diameter to the center-to-center distance of HFMs. The simulations were performed using different values for the R/a parameter, where the diameter of HFMs (R) and the feed and distillate velocities were kept constant. Figure 11(a) shows that the permeate flux drops when R/a becomes greater than 0.45. As shown in Figure 11(b), the permeate flux for a module with membranes that are 50 μm thick declined by 12 percent when R/a was increased from 0.4 to 0.49. This reduction in the flux is due to the overlapping of the thermal boundary layers, decreasing the temperature gradient across the membrane. Overlapping of the thermal boundary layers and increasing the transmembrane thermal conduction makes the process heat-transfer limited.

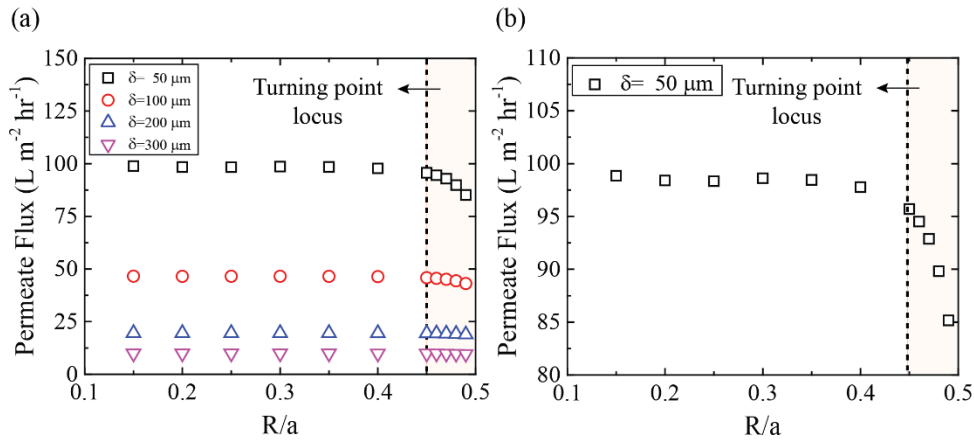


Figure 11. Effect of the interspacing parameter on the permeate flux: (a) the normalized permeate flux for membranes with various thicknesses; and (b) higher resolution data for a 50 μm thick membrane. Here, the outer radius of the membrane was kept constant at 400 μm . The feed and distillate inlet temperatures were 80°C and 17°C, respectively. The fiber porosity and tortuosity were set at 74% and 2.5, respectively. The length of the fibers was set to 4.5 cm. The shaded area, so-called turning point locus, represents the R/a values beyond which the flux declines rapidly.

3.1.3. Effect of Membrane Thickness

Mass and heat transfers in the membranes are two competing phenomena. It is well understood that having a higher temperature gradient across the membrane increases the mass transfer. On the other hand, a steeper temperature gradient increases the trans-membrane heat conduction. Both heat and mass transfer resistances increase with thickness; thus, it is important to find the dominating phenomena in the range of parameters used in our model.

Figure 12(a) shows the variation of the transmembrane temperature difference and permeate flux as a function of membrane thickness. Although the temperature difference increases, the permeate flux decreases with increased membrane thickness. Additionally, Figure 12(a) shows that the temperature gradient across the membrane does not change linearly with the membrane thickness. After reaching a certain value for membrane thickness, the slope of the temperature gradient diminishes. This phenomenon can be explained using the critical radius of insulation for cylindrical geometries. It is well known that the HFM acts as a thermal insulator between cold and hot streams, and as a result, the fiber thickness contributes to two competing phenomena. Increasing the thickness of the fiber results in the increase in the conductive heat transfer resistance, but at the same time enhances the area of heat transfer and reduces the convective heat transfer resistance. For this reason, we calculated the heat conduction and convection resistances at different values for membrane thickness. As shown in Figure 12(b), increasing the thickness increases the heat conduction resistance in the membrane and, at the same time, reduces the convective heat transfer resistance. Increasing the thickness above the critical value ($R_c = k_m/h_f$) diminishes the importance of the conductive heat transfer resistance; the heat transfer from the feed to the distillate becomes limited by the convective heat transfer resistance. This phenomenon explains the significant drop in the permeate flux, followed by a plateau as a function of membrane thickness shown in Figure 12(a). The theoretical value for the critical

insulation thickness for the HFMs ($k_m \sim 0.069 \text{ W/m K}$) under the current operating condition ($h_f \sim 5,800 \text{ W/m}^2 \text{ K}$) is around $12 \mu\text{m}$.

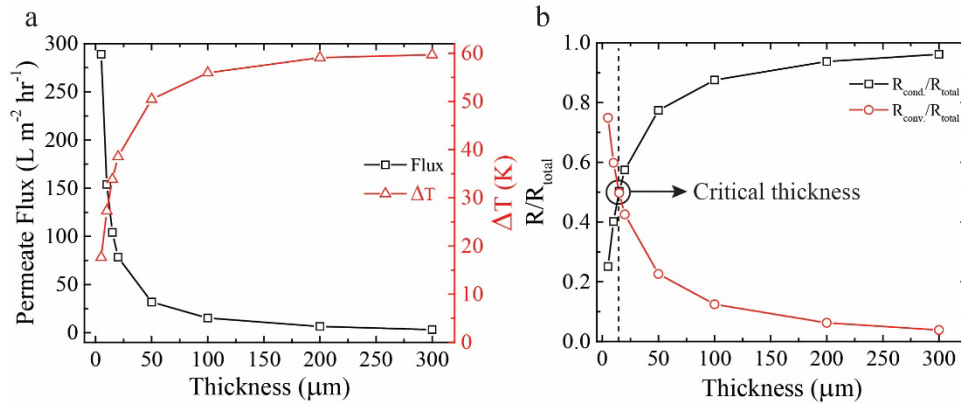


Figure 12. The effect of membrane thickness on performance. The effect of membrane thickness on the distillate flux and temperature difference across the membrane is shown in (a), and the ratio of conductive and convective heat transfer resistances to the total heat transfer resistance is shown in (b). The hollow fiber outer radius was kept constant at $400 \mu\text{m}$. The feed and distillate inlet temperatures were 17°C and 80°C , respectively. The fiber length, porosity, and tortuosity were set at 4.5 cm , 74% , and 2.5 , respectively.

3.1.4. Determining Membrane Diameter for the MD Module

The diameter of HFMs is another important factor affecting the SEC in an MD process. Membrane diameter influences both the pressure drops and the available mass transfer area in the module. In theory, for a single HFM, increasing the fiber diameter while keeping the thickness constant will increase the permeation flux (Porter 1989). However, increasing the diameter of fiber within a membrane package translates into a lower packing volume for the membrane module. For this reason, we studied the effect of the inner diameter of the HFM on the permeate flux while keeping the ratio of the outer diameter to the inner diameter constant at 1.33.

Figure 13(a) shows the dependence of permeate flux, normalized to the packing volume, and the total pressure drop in the module on the fiber radius. As can be seen, there are two regimes for this dependency. The rate of change in the permeate flux decreases with the increase in the inner radius of the fiber. At the low fiber radii, this change is more pronounced, which we attributed to the significant change in the pressure drop in the system ($\Delta p \propto R^{-2}$). After reaching a critical point for the fiber radius, the trade-off between enhanced surface area and the packing volume manifests itself, and the flux becomes invariable as a function of fiber internal radius. The critical inner radii of the HFMs with different lengths vary between $100 \mu\text{m}$ and $150 \mu\text{m}$; the critical inner radii increase for the longer HFMs. Additionally, in Figure 13(a), we see that the normalized permeate flux increases by one order of magnitude when the length of HFMs is decreased by 15 cm , from 20 cm to 4.5 cm .

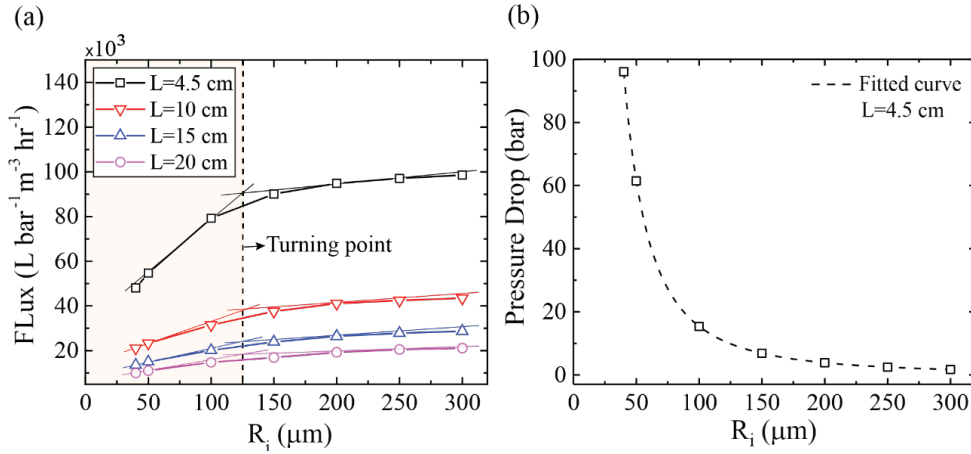


Figure 13. The effect of fiber inner diameter on the performance of packing. The effect of fiber inner diameter on the permeate flux, normalized by volume and pressure drop of the module, is shown in (a), and (b) shows the total pressure drop of the module ($L=4.5 \text{ cm}$). The ratio of external to internal radii of HFMs was kept constant at 1.33. Here, the velocity of feed and permeate were 1.6 m/s and 0.8 m/s , respectively. The feed and distillate inlet temperatures also were 17°C and 80°C , respectively. The interspacing parameter, fiber porosity, and tortuosity were set at 0.45, 74%, and 2.5, respectively. The shaded area represents the effective range of the inner diameter of HFMs.

In addition to the effect of pressure, the data presented in Figure 13(a) include the effect of HFM thickness on the permeate flux of the module. Hence, in Figure 13(b), we showed the effect of the HFM inner diameter on the pressure drop of the module separately. We found that compared to thickness, the effect of pressure drop (due to radius change) is dominant because it changes with the inverse square of the fiber radius ($\Delta p \propto R^{-2}$). However, our fitted curve on the thickness data in Figure 13(a) indicated that the permeate flux is dependent on the thickness of the HFM ($\delta=R_o-R_i$) with an inverse power of around one ($\text{flux} \propto \delta^{-0.94}$). Hence, for fiber radii lower than the critical range, the process in the MD module is limited by the pressure drop.

3.1.5. Effect of Feed and Distillate Velocities

Feed and distillate velocities are among the operating parameters in a DCMD process. A higher velocity inside the shell can increase the convective heat transfer coefficient, reducing the temperature polarization in the shell. Thus, adjusting feed and permeate velocities is necessary to control temperature polarization. Figure 14(a) and Figure 14(b) show the effect of feed and distillate velocities, respectively, on the permeate flux. The permeate flux is more sensitive to the velocity of feed compared to the distillate velocity because the heat transfer coefficient at the hot side is the determining parameter, influencing the thermal efficiency (e.g., temperature polarization) in the module. From Figure 14(a) we can deduce that the system is heat transfer limited at low feed velocity ranges (e.g., $V_f < 0.5 \text{ m/s}$). However, as the velocity increases, the convective heat transfer coefficient increases until the process becomes mass transfer limited; this change can be observed at velocities higher than 0.5. The dashed line in Figure 8(a) indicates the turning point.

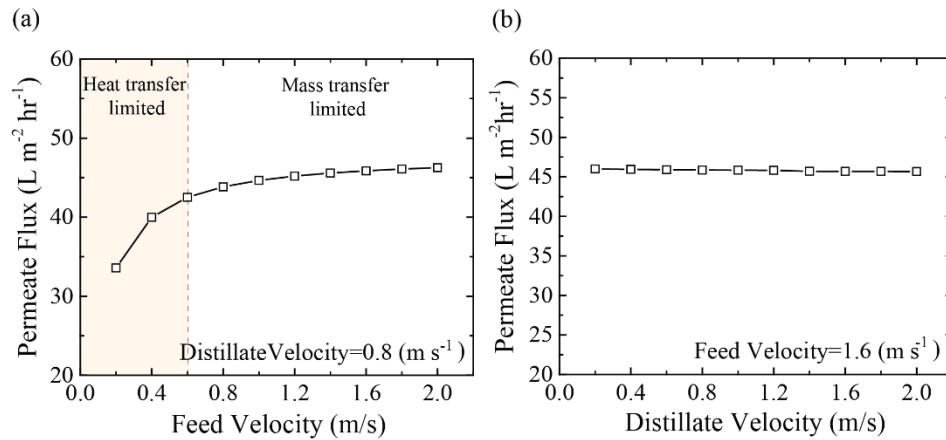


Figure 14. The effect of (a) feed stream velocity, and (b) distillate stream velocity on the normalized permeate flux. The membrane outer and inner radii were kept constant at 400 μm and 300 μm . The feed and distillate inlet temperatures were 17°C and 80°C, respectively. The fiber length, porosity, and tortuosity were set at 4.5 cm, 74%, and 2.5, respectively. Here, the inter-spacing parameter is 0.45.

3.1.6. Comparison of the Efficiency of Direct Contact Membrane Distillation (DCMD) with that of Sweeping Gas Membrane Distillation (SGMD).

After finishing the DCMD modeling work, we changed our model to evaluate the performance of our designed module under SGMD operation. We compared the result of the DCMD model to that of the SGMD model. Compared to DCMD, in the SGMD model, only one side of the membrane is in contact with a liquid stream, as airflow is used instead of the water distillate stream. To accurately model the transmembrane mass transfer in the SGMD process, we used the dusty gas model that takes into account the effect of viscous flow and the hydraulic pressure gradient across the membrane. Moreover, the impact of condensation coefficients across the membrane has been added to the models wherever a vapor-liquid interface exists. The condensation coefficients across the membrane are defined as interfacial resistance terms. In the SGMD process, an airstream sweeps the water vapor out of the module; therefore, no interfacial resistance was considered at the membrane-air interface.

Figure 15 compares the results of DCMD and SGMD models with respect to their thermal efficiencies and permeate fluxes. The SGMD process, on average, provides about 100 percent more flux than DCMD mode for all fiber interspacing parameters. This is due to higher thermal efficiency and less mass transfer resistance existing in SGMD compared to DCMD. According to Figure 15, the thermal efficiency of the SGMD process is also, on average 28 percent higher than that of DCMD. The thermal efficiency of the module was defined as the ratio of the heat used for water evaporation to the total heat provided to the module by the feed solution.

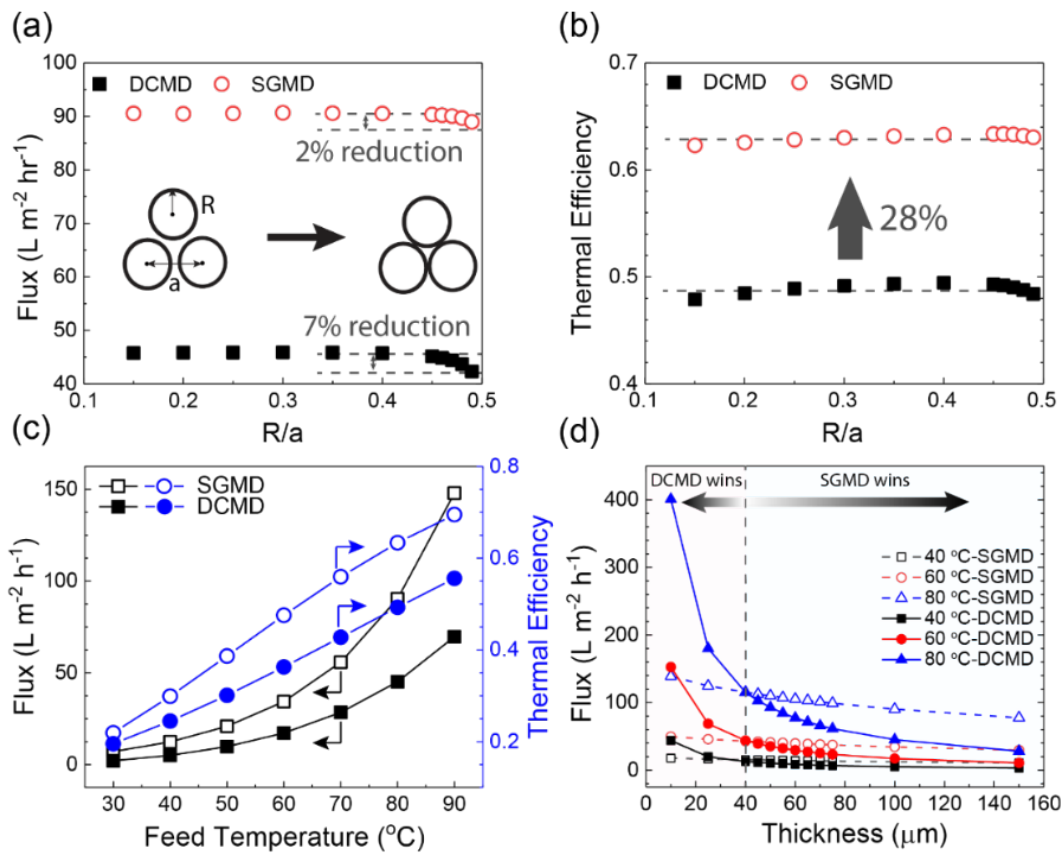


Figure 15. Comparison of DCMD and SGMD results: (a) the change in flux with fiber-to-fiber spacing (interspacing) distance; (b) the changes in the thermal efficiency of the module with fiber interspacing; (c) the variation of the permeate flux and thermal efficiency with the feed temperature; and (d) the effect of HFM thickness on permeate flux. In Figures 15a-c, the membrane thickness was assumed to be 100 μm ; the feed and distillate velocities were 0.08 m/s and 0.8 m/s, respectively.

Figure 15(c) compares the thermal efficiency and permeate flux of the DCMD and SGMD process at different feed temperatures. It can be seen that both energy efficiency and permeate flux increases with the temperature of the feed. This is because the changes in water flux with feed temperatures are nonlinear. The difference between SGMD and DCMD becomes more significant at higher feed temperatures due to high heat loss in DCMD at higher temperatures. Figure 15(d) illustrates the effect of membrane thickness on the permeate flux in DCMD and SGMD processes. The permeate flux increases when the membrane thickness decreases. The permeate flux of DCMD surpasses that of the SGMD process at thicknesses lower than approximately 40 μm . This shows that if the membrane thickness is maintained below 40 μm , the DCMD process is a better choice for water desalination by MD. Thus, we do not need to deal with the low efficiency of condensers used in the SGMD process to separate the water vapor from the air stream.

3.1.7. Design Optimization for Solar-Driven Hollow Fiber Modules

To study the performance of solar desalination using DCMD, we performed the thermodynamic analysis at the system level and used the estimated flux from our 3D modeling as an input. Thermodynamic performance can be described by the efficiency derived from the second law of thermodynamics. Since membrane distillation is a thermally-driven process, its efficiency can be related to the generation of entropy in the major components of the system, including module, cooler and heater, and solar collector (detailed derivation of governing thermodynamic equations is described in Appendix B). Using the governing thermodynamic equations, we studied how different processes and design parameters influence the thermodynamic performance of solar-assisted membrane distillation. For instance, the length of the DCMD module affects the flux by influencing heat and mass transport between the feed and distillate streams. As illustrated in Figure 16, modules with a higher length provide lower flux due to the reduction in driving force between the two interfaces of the membrane along its length. On the other hand, longer modules have a higher water production rate, which leads to a significant reduction in specific entropy generation associated with the DCMD module, as shown in Figure 16.

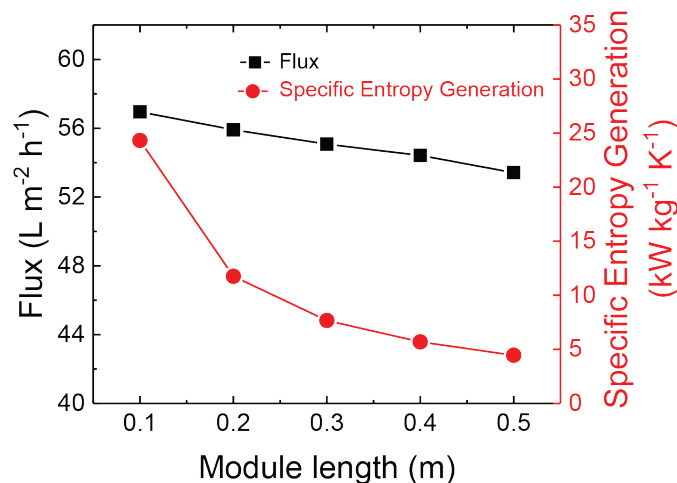


Figure 16. The effect of module length on the flux and specific entropy generation of DCMD module. The flux was obtained from COMSOL and specific entropy generation was calculated using Equations A8 and A17. The simulation was performed for feed and distillate temperatures of 80 °C and 20 °C, respectively.

We estimated that for a water production capacity of 2 m³ day⁻¹ and feed and distillate temperature of 80 °C and 20 °C, respectively, the total entropy generation is 2,871.2 J kg⁻¹ K⁻¹ and the second law efficiency is 12.92 percent. In such a system, the solar collectors are the primary source of entropy generation, as illustrated in Figure 17. This is due to the inefficiency of the collector that leads to thermal energy losses. Also, the difference between the sun's apparent temperature and the collectors' working temperature leads to high entropy generation rates. The DCMD module and heat exchanger are the other two significant contributors to entropy generation. Entropy generation due to stream temperature disequilibrium with the environment was negligible.

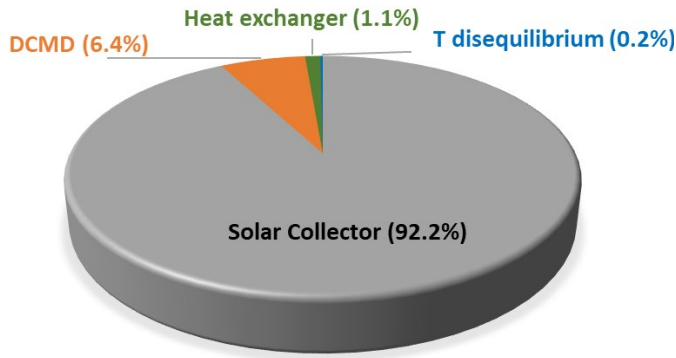


Figure 17. The relative contribution of each entropy generation source to the total entropy generation of solar MD system. The total specific entropy generation is $2871.2 \text{ J kg}^{-1} \text{ K}^{-1}$ and the corresponding second law efficiency is 12.92 percent. Calculations were performed using analyses in Appendix C.

In addition, we evaluated the system under different climate conditions as illustrated in Figure 18. The calculations were performed based on a module 2 cm in diameter and 9 cm in length, containing 135 fibers. The heat source to the feed was obtained from a flat plate solar collector with an area of 15 m^2 and the auxiliary heater that provides heat duty during nighttime. We used metrological data obtained from the National Renewable Energy Lab (NREL) for Lincoln, Nebraska to predict the change in flux throughout the day. Figure 18(a) and Figure 18(b) show the behavior of flux during a typical summer and winter day. The total water produced was 16.4 and 7.3 L/day for a summer and winter day, respectively.

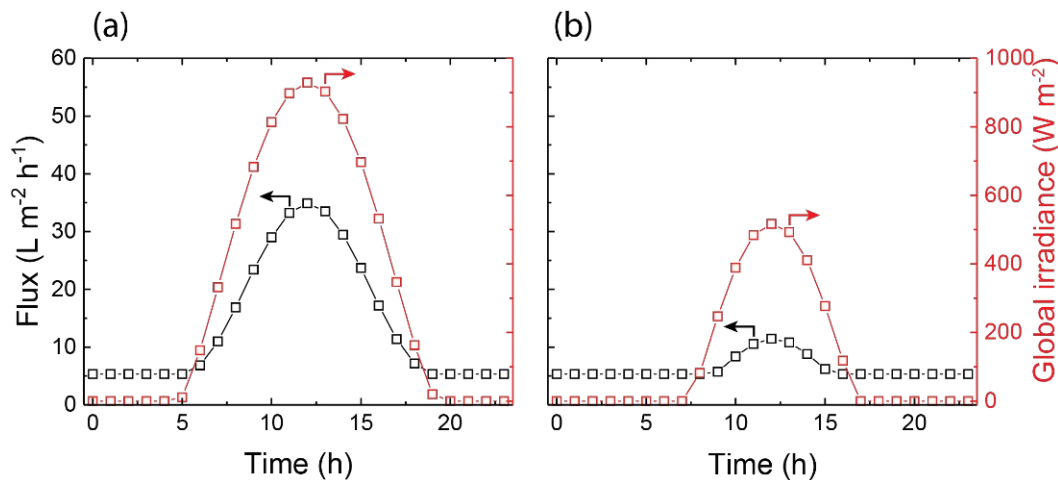


Figure 18. The global irradiance on a flat surface and the corresponding DCMD flux in a typical day: (a) summer day; and (b) winter day. Metrological data were obtained from the NREL National Solar Radiation Database. The simulated results were taken for July 24 and January 17, 2017.

3.2. Model Validation and Fabrication of Prototype HFM Modules

The temperature of the feed stream has a significant effect on the performance of the MD module because this temperature directly influences the temperature difference across the membrane. Figure 19 presents the effect of feed temperature on the permeate flux for close-packed modules having membranes with different porosities, 74 percent (HFM-A) and 68 percent (HFM-B). The experimental data were taken from Wang et al. (2008). The results indicate that the permeate flux increases with increasing feed temperature. However, the permeate flux for the HFM-A membrane is significantly higher than that for the HFM-B membrane. As shown in the inset of Figure 19, the structures of these membranes are significantly different. Membrane HFM-B is more porous and has macrovoids in its structure, while membrane HFM-A is cellular in structure and appears to have less pore volume. It is expected that the structural characteristics of the membranes play a critical role in membrane performance (Deshmukh and Elimelech 2017). Because the tortuosity values for the HFM-A and HFM-B membranes were not reported, we validated our model by sweeping the simulations over a range of the tortuosity parameters. According to Figure 19(a) and Figure 19(b), the simulation results for HFM-A and HFM-B agreed with the experimental results when the tortuosity values of 2.5 and 8 were used in the model.

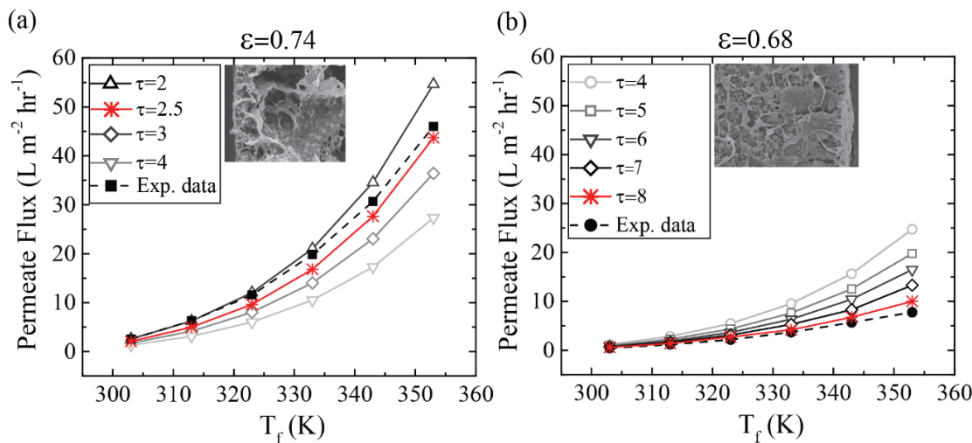


Figure 19. A comparison between experimental and computational results. The comparison was done regarding the distillate flux of two HFMs, the prediction of the model at comparable porosities (74% and 68%), and a range of tortuosity factor (τ) for the membranes in a close-packed configuration. The membrane structure, properties, and all parameters describing the geometry and operating conditions are taken from Wang et. al (2008). Results shown in (a) represent high porosity and low tortuosity membrane; results shown in (b) represent lower porosity and higher tortuosity membranes. Here, feed velocity is 1.6 m/s; distillate velocity is 0.8 m/s; fiber length, inner diameter, and outer diameter are 20 cm, 600 μm , and 800 μm , respectively. The distillate temperature and fiber inter-spacing parameters are 17°C and 0.45, respectively.

3.2.1. Fabricating Hollow Fiber Membranes

Equipped with the knowledge of performance as a function of geometrical and physical parameters of the system, we made HFMs for our module fabrication. Through the design of our experiment, we formulated the dope solution composition and identified the dry-jet spinning parameters to fabricate HFMs with dual skin layers. The outer and inner skin of the fiber appears to be denser than the bulk of the fiber. This is due to the relatively faster precipitation rate at the boundary of the polymer solution and coagulants. Figure 20 shows a representative SEM image of an HFMs used for module fabrication.

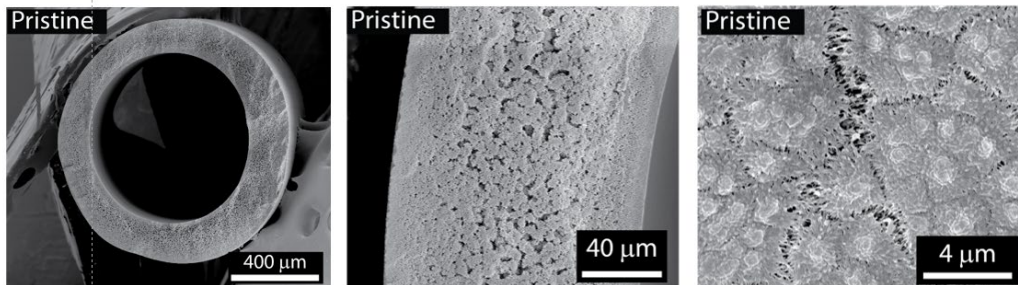


Figure 20. Cross-section and top-down SEM images of HFMs

3.2.1.1. Post-Processing of HFMs

Figure 21 shows a cross-section SEM image of the HFMs that were modified by developing a surface modification approach, based on iCVD (see Appendix C). Here the reentrant structures created on the outer surface of an HFM can be seen in Figure 21c. The importance of reentrant superhydrophobic structure on the robustness in the performance of the HFM modules and the reduction in the scaling propensity of the surface was the driving force for this development.

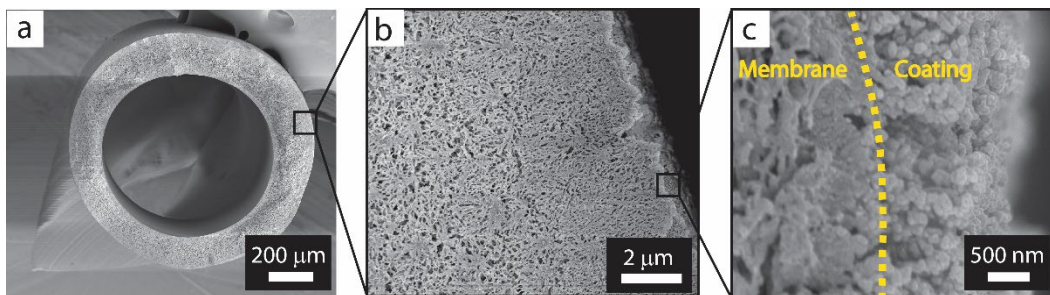


Figure 21. Cross-section SEM images of modified HFMs. Reentrant structures are created to reduce the surface energy by deposition of particulate structures of PTFE and a conformal layer of PPFDA on the surface of the HFM.

We measured the mean pore size of the outer surface of the hollow fibers to be approximately $0.11 \mu\text{m}$ using image analysis (ImageJ), shown in Figure 22. As shown, the average surface porosity of HFMs did not change significantly after iCVD coating. This is because the deposited PTFE structure is highly porous and so does not add any significant resistance for vapor permeation. The comparison of N_2 permeation for the pristine and functionalized HFMs, shown

in Figure 23, is consistent with the finding that the porous PTFE coating did not significantly reduce the surface porosity.

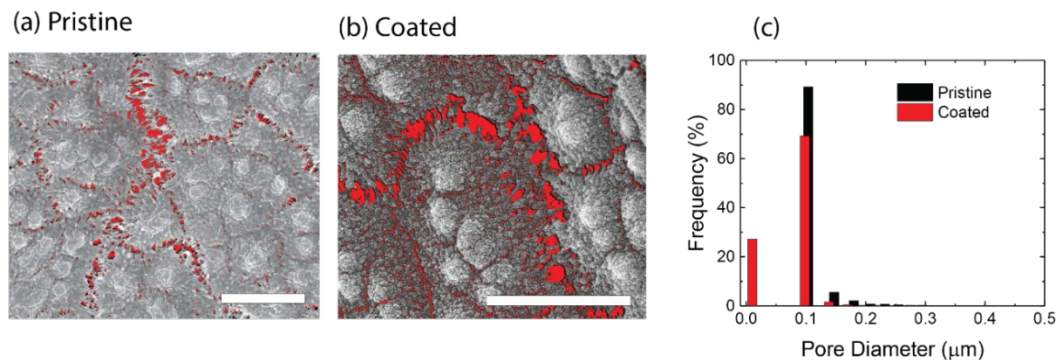


Figure 22. Top-down SEM image of (a) pristine and (b) coated HFM. Scale bars in (a) and (b) are 4 and 5 μm . The plot in (c) shows pore size distribution using image analysis on (a) and (b). The mean pore sizes for the pristine and coated HFM were 0.11 and 0.077 μm , respectively.

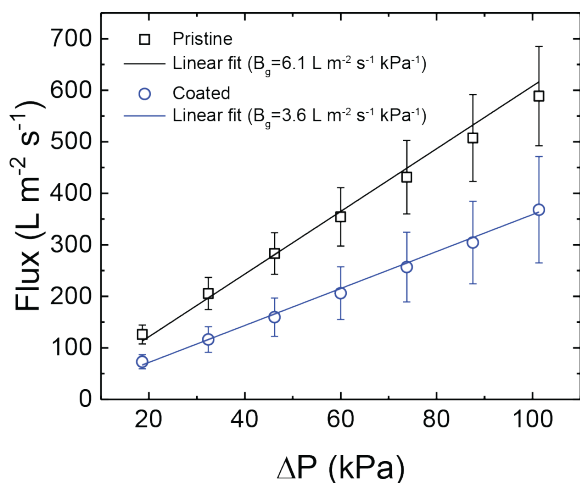


Figure 23. Gas permeation of the pristine and coated HFM. The correlation factors, R^2 , for the pristine and coated HFM were 0.9966 and 0.9972, respectively.

3.2.2. Spacer Fabrication and Assembly

Using the optimal results of the modeling, we fabricated a module that replicates the geometry of the simulation. We were able to build the desired module with controlled spacing between the fibers by making module spacers using the additive manufacturing (3D printing) approach. As illustrated in Figure 24, PVDF HFMs were passed through the holes of two spacers and the modules were assembled. Accordingly, the inlet and outlet to the shell side of the module were created by drilling two holes, threading them, and connecting a tube and hose fitting. The inlet and outlet of the lumen were formed by threading the two edges of the plastic tube and connecting them with two adaptors with the correct fittings. We also made modules with 120 HFMs packed in place as illustrated in Figure 24. The size of these modules was 3.2 cm inside diameter and 10 cm in length. This module can desalinate about 45 L/day of water if the feed

and distillate temperatures are kept constant at 70°C and 20°C, respectively. The packing density of the HFM bundle was 3600 m²/m³.

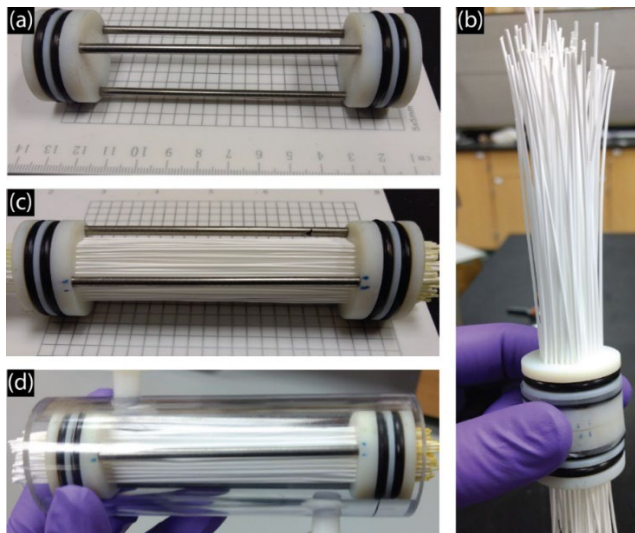


Figure 24. Assembling steps of a module consisting of more than 120 number of HFMs: (a) the 3D printed spacers with two rubber O-rings; (b) the 3D-printed spacer after making the organized packing configuration; (c) an assembled version of HFM bundle; and (d) a complete example of the prototype. The packing density of the shown bundle is 3600 m²/m³.

3.3. Characterization of the Fabricated Modules under Various Operation Modes

To investigate the desalination performance of the pristine and coated membranes with low surface energy feed water, we added 0.1, 0.2, 0.3, and 0.4 mM SDS to the 0.3 M NaCl feed at 50°C to lower the surface tension to approximately 54, 47, 43, and 39 mN m⁻¹, respectively (Matijević and Pethica 1958). The HFMs were tested with surfactants and oil in a saline feed solution. The effect of surfactants was studied by sequentially adding SDS to the 0.3 M NaCl feed with an increment of 0.1 mM every hour until the concentration reached 0.4 mM. Neither the pristine nor the coated hollow fibers showed any sign of wetting throughout the 9 hours of DCMD operation, as displayed in Figure 25(d). Both membranes maintained a normalized flux close to unity and an approximate 100 percent salt rejection.

The wetting resistance of the HFMs can be attributed to two reasons. Firstly, the small pore size of the outer surface of the fibers leads to a higher value of liquid entry pressure. Even though the surface tension at the liquid-gas interface decreased due to the presence of SDS, it was not enough to induce the penetration of water into small pores. Secondly, the tail of the surfactant adsorbs to the surface of the membrane surface due to nonpolar (hydrophobic) interactions between the molecules of the surfactant and the polymer. This lowers the number of surfactant molecules near the liquid-gas interface at the vicinity of the pore, which consequentially increases the surface tension compared to the bulk (Wang et al. 2018).

To test the omniphobic membranes in desalination of oil-contaminated water solutions, we prepared synthetic oil emulsion. Canola oil with concentrations of 100 and 500 ppm was vigorously stirred in 0.3 M NaCl and 0.07 mM SDS solution for 1 hour before starting the DCMD experiment. The SDS was added to stabilize the oil droplets and create an emulsion. The oil droplets were analyzed using an optical microscope (Axio Lab.A1, Zeiss, USA). As shown in Figure 25 (a-c), the droplet size distribution was determined by using image analysis of the micrographs taken by an optical microscope. The DCMD results in Figure 25(e) and Figure 25(f) showed that, when the amount of contamination was 100 ppm, no fouling was observed for either pristine or functionalized membranes. However, in the case of 500 ppm contamination, the salt rejection of the pristine membrane was dropped, meaning that a complete wetting occurred. However, the salt rejection for the omniphobic HFM remained at 100 percent. The reduction in the flux of the omniphobic membrane shows that partial wetting and fouling occurred on the surface.

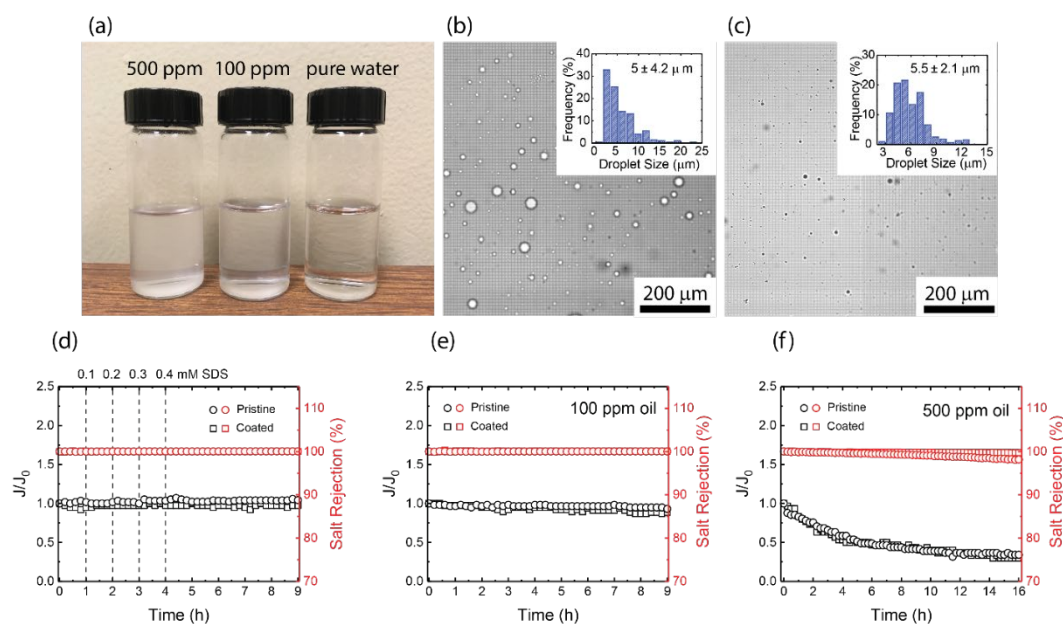


Figure 25. Membrane distillation results of samples including oil contamination. The photograph in (a) shows water samples of 500 ppm, 100 ppm oil, and pure water. Optical microscopic images of 500 ppm oil emulsion and 100 ppm oil emulsion are shown in (b) and (c), respectively. The insets in (b) and (c) display the size of oil droplets using image analysis on the micrographs. Normalized water flux and salt rejection of the pristine membrane ($\phi=9.3\%$) and the coated membrane ($\phi=9.3\%$) are shown in (d), varying concentration of SDS in the feed, in (e) for 100 ppm oil, and in (f) for 500 ppm oil. The feed and distillate temperatures were set to 50°C and 19°C , respectively. The flow rate of feed and distillate was set to 0.4 L min^{-1} . J_0 of the pristine and coated membranes were (d) 14.3 and $9.25 \text{ L m}^{-2} \text{ h}^{-1}$, (e) 14.5 and $9.5 \text{ L m}^{-2} \text{ h}^{-1}$, and (f) 10.25 and $8.15 \text{ L m}^{-2} \text{ h}^{-1}$, respectively.

We studied the effect of surface functionalization on the salt scaling propensity on the outer surface of HFMs through an accelerated salt scaling experiment. For this purpose, the membranes were glued to a glass slide and immersed in a 20 mM CaCl_2 and Na_2SO_4 solution. The solution was capped, heated to 60°C while stirring at 300 revolutions per minute for 24

hours. Then the HFMs were removed from the solution and dried at room temperature. Finally, the surfaces of the membranes were analyzed with SEM. The SEM images of the pristine and functionalized membrane after the scaling experiment are displayed in Figure 26(a) and Figure 26(b), respectively. The results show a clear difference in size and area fraction of the crystals deposited on the pristine and coated membrane. The area fraction of salt crystals on the pristine surface was 19.7 percent of the membrane surface area as shown in Figure 26(a), while the area fraction was less than 3 percent for the functionalized membrane surface, as shown in Figure 26(b). The heterogeneous nucleation of gypsum crystals on a surface is dependent on the wettability of the surface; low surface wettability indicates low interaction between the surface and the crystal (Karanikola et al. 2018; Su et al. 2018). We showed that the wettability of the hollow fibers decreased after coating them with PTFE and PPFDA. Therefore, we attribute this reduction in crystal formation to the reduced wettability of the surface.

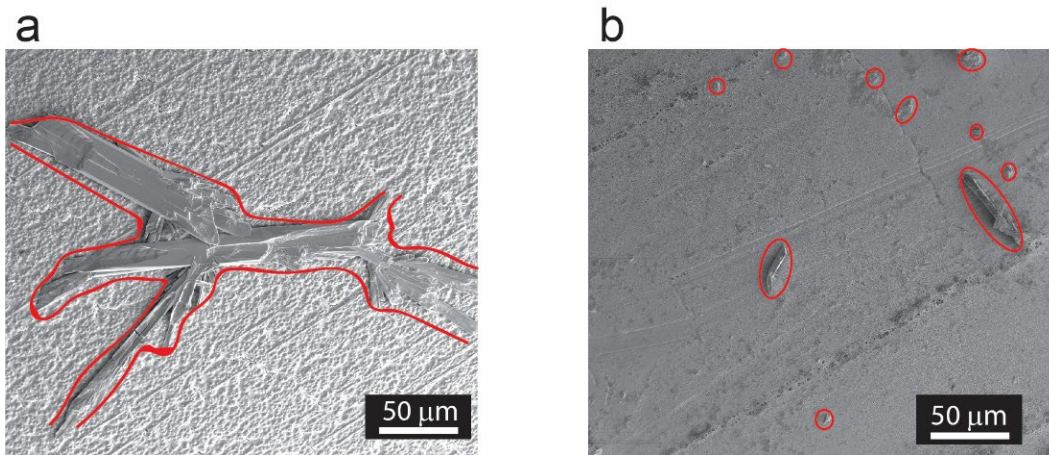


Figure 26. SEM images of outer surfaces of membranes for (a) pristine and (b) functionalized HFM after accelerated salt scaling experiment. The salt crystals on membranes are circled with a red line.

We fabricated modules in different sizes and tested them in different conditions. To validate the simulation results, we performed the DCMD process at different feed temperatures (40-70°C). Figure 27 shows the effect of temperature and module packing density on water production rate per volume of packing. Increasing the packing density of the module increases the water production rate due to an increase in membrane surface area.

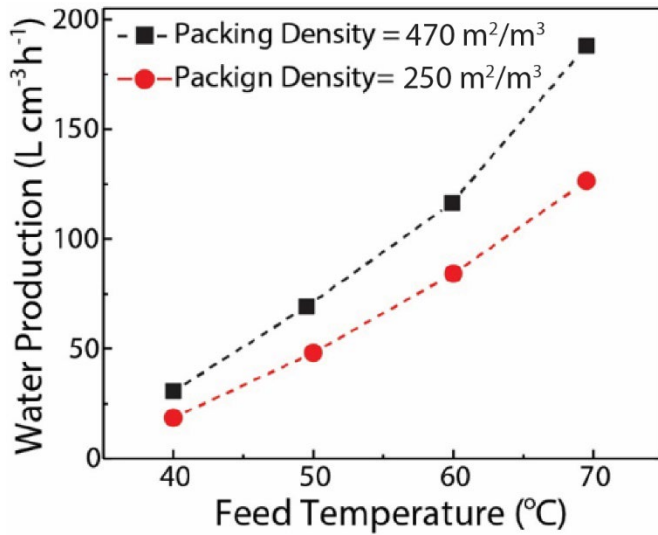


Figure 27. The effect of feed temperature on the water production rate per volume of modules with different packing densities.

To confirm the modeling results, we designed sets of experiments and performed simulations at the same conditions. Figure 28(a) shows the effect of feed temperature on permeate flux for a module with a 250 m²/m³ packing density. Simulations and experimental results agree; they show a similar trend for permeate flux as a function of feed temperature. Figure 28(b) illustrates the effect of feed velocity on the permeate flux. The simulation and experimental results follow a similar trend. There is an offset between the experimental and simulation, and we attribute this to the end effects as the module is very short in length. At the lower velocities, the system is heat transfer limited; as a result, more deviation is observed between predicted and experimental results.

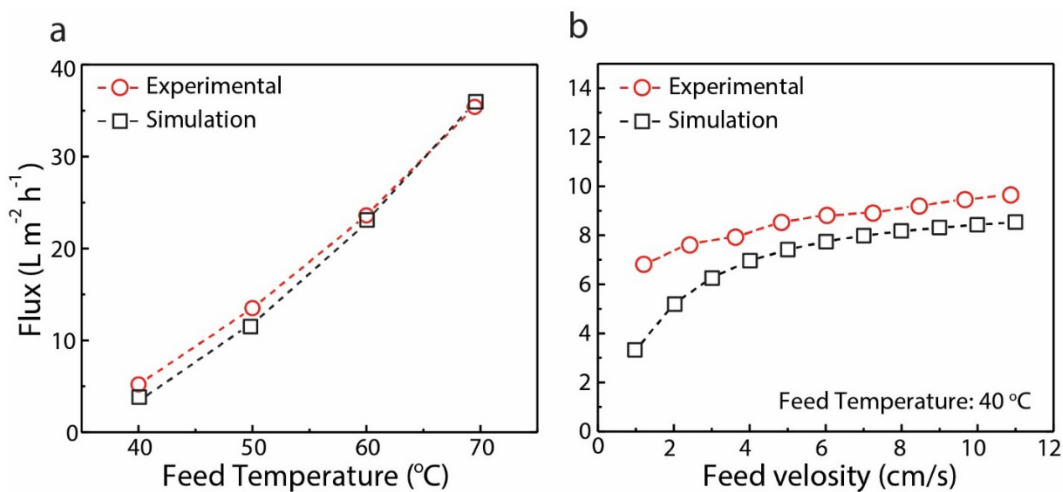


Figure 28. Comparison of experimental and simulations results. The plot in (a) shows the effect of feed temperature on the permeation flux. Here, the packing density of the module was 250 m²/m³, and feed and distillate velocities were set at 0.01 and 0.8 m/s, respectively. The plot in (b) shows the effect of feed velocity on the permeate flux. Here, the feed temperature was set at 40°C.

4. Conclusion

4.1. Outcomes

A model-guided approach was developed to design and fabricate a solar-integrated HFM system. For this reason, a multiphysics model was utilized to predict and optimize the performance of HFM modules with respect to their water production and energy efficiency. Using additive manufacturing, we printed spacers to direct the flow in the feed channel of the modules and packed membranes into the desired geometrical arrangement. We were able to validate our modeling prediction and fabricated HFM modules with a robust performance in the various and challenging feed streams. We performed a system-level analysis for the mass and energy balance over a solar-integrated MD scheme. Our modeling analysis indicates that for approximately 150 fibers packed in a module with a packing density and length of $3,600 \text{ m}^2/\text{m}^3$ (module length: 10 cm), 50 L per day of deionized water can be collected, utilizing the solar energy for heating water. The SEC for such a scheme is rated below $10 \text{ kWh}/\text{m}^3$.

4.2. Recommended next steps

For the next step of this project, we plan to assemble a pilot-scale solar collector for heating the water and power the pumps using photovoltaic modules. We expect, with a proper control scheme, we could provide enough deionized water for a household of five. We plan to perform techno-economic and life-cycle analysis and design a technology-to-market plan, considering all aspects of the process; the control scheme and automation will be among the objectives of the next step. We are considering having our design based on the brine output of the RO plant located in Hasting, Nebraska. We plan to build a pilot-scale model at our innovation campus at the University of Nebraska-Lincoln. Additionally, to protect this development, we expect to file a patent on membrane and module fabrication and another on the process design.

References

- Alkhudhiri, A., N. Darwish, and N. Hilal. 2012. "Membrane Distillation: A Comprehensive Review." *Desalination* 287, pp. 2–18. doi:10.1016/j.desal.2011.08.027.
- Amy, G., N. Ghaffour, Z. Li, L. Francis, R.V. Linares, T. Missimer, and S. Lattemann. 2017. "Membrane-Based Seawater Desalination: Present and Future Prospects." *Desalination* 401, pp. 16–21. doi:10.1016/j.desal.2016.10.002.
- Azari, A., M.A. Abbasi, and H. Sanaeepur. 2016. "CFD Study of CO₂ Separation in an HFMC Under Non-Wetted and Partially-Wetted Conditions." *Int. J. Greenb. Gas Control* 49, pp. 81–93.
- Banat, F., R. Jumah, and M. Garaibeh. 2002. "Exploitation of Solar Energy Collected by Solar Stills for Desalination by Membrane Distillation." *Renew. Energy* 25, pp. 293–305.
- Bao, L. and G. Lipscomb. 2002. "Mass Transfer in Axial Flows through Randomly Packed Fiber Bundles with Constant Wall Concentration." *J. Memb. Sci.* 204, pp. 207–220. doi:10.1016/S0376-7388(02)00043-1.
- Bejan, A., D.W. Kearney, and F. Kreith. 1981. "Second Law Analysis and Synthesis of Solar Collector Systems." *J. Sol. Energy Eng.* 103, p. 23. doi:10.1115/1.3266200.
- Bonyadi, S. and T.-S.S. Chung. 2009. "Highly Porous and Macrovoid-Free PVDF Hollow Fiber Membranes for Membrane Distillation by a Solvent-Dope Solution Co-Extrusion Approach." *J. Memb. Sci.* 331, pp. 66–74. doi:10.1016/j.memsci.2009.01.014.
- Boo, C., J. Lee, and M. Elimelech. 2016. "Omniphobic Polyvinylidene Fluoride (PVDF) Membrane for Desalination of Shale Gas Produced Water by Membrane Distillation." *Environ. Sci. Technol.* 50, pp. 12275–12282. doi:10.1021/acs.est.6b03882.
- Chafidz, A., E.D. Kerme, I. Wazeer, Y. Khalid, A. Ajbar, and S.M. Al-Zahrani. 2016. "Design and Fabrication of a Portable and Hybrid Solar-Powered Membrane Distillation System." *J. Clean. Prod.* 133, pp. 631–647. doi:http://dx.doi.org/10.1016/j.jclepro.2016.05.127.
- Chang, J., J. Zuo, L. Zhang, G.S. O'Brien, and T.-S. Chung. 2017. "Using Green Solvent, Triethyl Phosphate (TEP), to Fabricate Highly Porous PVDF Hollow Fiber Membranes for Membrane Distillation." *J. Memb. Sci.* 539, pp. 295–304. doi:10.1016/j.memsci.2017.06.002.
- Chen, V. and M. Hlavacek. 1994. "Application of Voronoi Tessellation for Modeling Randomly Packed Hollow-Fiber Bundles." *AIChE J.* 40, pp. 606–612. doi:10.1002/aic.690400405.
- Coclite, A.M., R.M. Howden, D.C. Borrelli, C.D. Petruczok, R. Yang, J.L. Yagüe, A. Ugur, N. Chen, S. Lee, and W.J. Jo. 2013. "25th Anniversary Article: CVD Polymers: A New Paradigm for Surface Modification and Device Fabrication." *Adv. Mater.* 25, pp. 5392–5423.

- Deshmukh, A. and M. Elimelech. 2017. “Understanding the Impact of Membrane Properties and Transport Phenomena on Energetic Performance of Membrane Distillation Desalination.” *J. Memb. Sci.* doi:10.1016/j.memsci.2017.05.017.
- Deshmukh, A. and J. Lee. 2019. “Membrane Desalination Performance Governed by Molecular Reflection at the Liquid-Vapor Interface.” *Int. J. Heat Mass Transf.* 140, pp. 1006–1022. doi:10.1016/j.ijheatmasstransfer.2019.06.044.
- Ding, Z., L. Liu, M.S. El-Bourawi, and R. Ma. 2005. “Analysis of a Solar-Powered Membrane Distillation System.” *Desalination* 172, pp. 27–40.
- Feng, C.Y.Y., K.C.C. Khulbe, T. Matsuura, and A.F.F. Ismail. 2013. “Recent Progresses in Polymeric Hollow Fiber Membrane Preparation, Characterization and Applications.” *Sep. Purif. Technol.* 111, pp. 43–71. doi:10.1016/j.seppur.2013.03.017.
- Gates, J.B., J.P. Nicot, B.R. Scanlon, and R.C. Reedy. 2011. Arsenic Enrichment in Unconfined Sections of the Southern Gulf Coast Aquifer System, Texas.” *Appl. Geochemistry* 26, pp. 421–431. doi:10.1016/J.APGEOCHEM.2011.01.002.
- Ghaffour, N., T.M. Missimer, and G.L. Amy. 2013. “Technical Review and Evaluation of the Economics of Water Desalination: Current and Future Challenges for Better Water Supply Sustainability.” *Desalination* 309, pp. 197–207.
- Ghaleni, M.M., S. Kaviani, M. Bavarian, and S. Nejati. 2019. “Bottom-Up Fabrication of Flexible and Porous Omniphobic Interfaces Via Sequential Initiated Chemical Vapor Deposition.” *AIChE Annu. Meet.*
<https://aiche.confex.com/aiche/2019/meetingapp.cgi/Paper/578115> (accessed February 17, 2020).
- Giaya, A. and R.W. Thompson. 2002. “Water Confined in Cylindrical Micropores.” *J. Chem. Phys.* 117, pp. 3464–3475. doi:10.1063/1.1494419.
- Gleason, K.K. 2019. “From Chemical Engineering Fundamentals to the Commercialization of Vapor Deposited Polymers.” *AIChE Annu. Meet.*
<https://aiche.confex.com/aiche/2019/meetingapp.cgi/Paper/579451>.
- Haase, M.F., K.J. Stebe, and D. Lee. 2015. “Continuous Fabrication of Hierarchical and Asymmetric Bijel Microparticles, Fibers, and Membranes by Solvent Transfer-Induced Phase Separation (STRIPS).” *Adv. Mater.* 27, pp. 7065–7071.
- Hogan, P.A., Sudjito, A.G. Fane, and G.L. Morrison. 1991. “Desalination by Solar Heated Membrane Distillation.” *Desalination* 81, pp. 81–90. doi:http://dx.doi.org/10.1016/0011-9164(91)85047-X.
- Hou, D., J. Wang, C. Zhao, B. Wang, Z. Luan, and X. Sun. 2010. “Fluoride Removal from Brackish Groundwater by Direct Contact Membrane Distillation.” *J. Environ. Sci.* 22, pp. 1860–1867.
- Kalogirou, S.A. 2004. “Solar Thermal Collectors and Applications.” *Prog. Energy Combust. Sci.* 30, pp. 231–295.

- Karanikola, V., A.F. Corral, H. Jiang, A. Eduardo Sáez, W.P. Ela, and R.G. Arnold. 2015. “Sweeping Gas Membrane Distillation: Numerical Simulation of Mass and Heat Transfer in a Hollow Fiber Membrane Module.” *J. Memb. Sci.* 483, pp. 15–24. doi:<http://dx.doi.org/10.1016/j.memsci.2015.02.010>.
- Karanikola, V., A.F. Corral, H. Jiang, A.E. Sáez, W.P. Ela, and R.G. Arnold. 2017. “Effects of Membrane Structure and Operational Variables on Membrane Distillation Performance.” *J. Memb. Sci.* 524, pp. 87–96.
- Karanikola, V., C. Boo, J. Rolf, and M. Elimelech. 2018. “Engineered Slippery Surface to Mitigate Gypsum Scaling in Membrane Distillation for Treatment of Hypersaline Industrial Wastewaters.” *Environ. Sci. Technol.* 52, pp. 14362–14370. doi:10.1021/acs.est.8b04836.
- Kast, W. and C.-R.R. Hohenthanner. 2000. “Mass Transfer within the Gas-Phase of Porous Media.” *Int. J. Heat Mass Transf.* 43, pp. 807–823. doi:10.1016/S0017-9310(99)00158-1.
- Kavvadias, K.C. and I. Khamis. 2014. “Sensitivity Analysis and Probabilistic Assessment of Seawater Desalination Costs Fueled by Nuclear and Fossil Fuel.” *Energy Policy* 74, pp. S24–S30. doi:<http://dx.doi.org/10.1016/j.enpol.2014.01.033>.
- Khayet, M., M.P. Godino, and J.I. Mengual. 2003a. “Possibility of Nuclear Desalination through Various Membrane Distillation Configurations: a Comparative Study.” *Int. J. Nucl. Desalin.* 1, pp. 30–46.
- Khayet, M., M.P. Godino, and J.I. Mengual. 2003b. “Theoretical and Experimental Studies on Desalination using the Sweeping Gas Membrane Distillation Method.” *Desalination* 157, pp. 297–305. doi:[http://dx.doi.org/10.1016/S0011-9164\(03\)00409-0](http://dx.doi.org/10.1016/S0011-9164(03)00409-0).
- Khayet, M.S. and T. Matsuura. 2011. *Membrane Distillation : Principles and Applications*. Elsevier, 2011.
- Khayet, M. 2013. “Solar Desalination by Membrane Distillation: Dispersion in Energy Consumption Analysis and Water Production Costs (a Review).” *Desalination* 308, pp. 89–101.
- Kim, Y.-D., K. Thu, N. Ghaffour, and K. Choon Ng. 2013. “Performance Investigation of a Solar-Assisted Direct Contact Membrane Distillation System.” *J. Memb. Sci.* 427, pp. 345–364. doi:<http://dx.doi.org/10.1016/j.memsci.2012.10.008>.
- Kim, Y.-D., K. Thu, K.C. Ng, G.L. Amy, and N. Ghaffour. 2016. “A Novel Integrated Thermal-/Membrane-Based Solar Energy-Driven Hybrid Desalination System: Concept Description and Simulation Results.” *Water Res.* 100, pp. 7–19.
- Koschikowski, J., M. Wieghaus, and M. Rommel. 2003. Solar Thermal Driven Desalination Plants Based on Membrane Distillation.” *Water Sci. Technol. Water Supply* 3, pp. 49–55.
- Koutsou, C.P., A.J. Karabelas, and M. Kostoglou. 2015. “Membrane Desalination under Constant Water Recovery – the Effect of Module Design Parameters on System

- Performance.” *Sep. Purif. Technol.* 147, pp. 90–113.
doi:<http://dx.doi.org/10.1016/j.seppur.2015.04.012>.
- Lau, K.K.S., J. Bico, K.B.K. Teo, M. Chhowalla, G.A.J. Amaratunga, W.I. Milne, G.H. McKinley, and K.K. Gleason. 2003. “Superhydrophobic Carbon Nanotube Forests.” *Nano Lett.* 3, pp. 1701–1705.
- Lawson, K.W. and D.R. Lloyd. 1997. “Membrane Distillation.” *J. Memb. Sci.* 124, pp. 1–25.
doi:[10.1016/S0376-7388\(96\)00236-0](https://doi.org/10.1016/S0376-7388(96)00236-0).
- Lee, J. and R. Karnik. 2010. “Desalination of Water by Vapor-Phase Transport Through Hydrophobic Nanopores.” *J. Appl. Phys.* 108. doi:[10.1063/1.3419751](https://doi.org/10.1063/1.3419751).
- Lee, J., T. Laoui, and R. Karnik. 2014. “Nanofluidic Transport Governed by the Liquid/Vapour Interface.” *Nat. Nanotechnol.* 9, pp. 317–23. doi:[10.1038/nnano.2014.28](https://doi.org/10.1038/nnano.2014.28).
- Lee, J., C. Boo, W.-H. Ryu, A.D. Taylor, and M. Elimelech. 2016. “Development of Omniphobic Desalination Membranes Using a Charged Electrospun Nanofiber Scaffold.” *ACS Appl. Mater. Interfaces* 8, pp. 11154–11161. doi:[10.1021/acsami.6b02419](https://doi.org/10.1021/acsami.6b02419).
- Li, L. and K.K. Sirkar. 2016. “Influence of Microporous Membrane Properties on the Desalination Performance in Direct Contact Membrane Distillation.” *J. Memb. Sci.* 513, pp. 280–293. doi:[10.1016/j.memsci.2016.04.015](https://doi.org/10.1016/j.memsci.2016.04.015).
- Lian, B., Y. Wang, P. Le-Clech, V. Chen, and G. Leslie. 2016. “A Numerical Approach to Module Design for Crossflow Vacuum Membrane Distillation Systems.” *J. Memb. Sci.* 510, pp. 489–496. doi:<http://dx.doi.org/10.1016/j.memsci.2016.03.041>.
- Lienhard, J.H., K.H. Mistry, M.H. Sharqawy, and G.P. Thiel. 2017. “Chapter 4 – Thermodynamics, Exergy, and Energy Efficiency in Desalination Systems” in: *Desalin. Sustain.*, pp. 127–206. doi:[10.1016/B978-0-12-809791-5.00004-3](https://doi.org/10.1016/B978-0-12-809791-5.00004-3).
- Lin, S., S. Nejati, C. Boo, Y. Hu, C.O. Osuji, and M. Elimelech. 2014. “Omniphobic Membrane for Robust Membrane Distillation.” *Environ. Sci. Technol. Lett.* 1, pp. 443–447.
doi:[10.1021/ez500267p](https://doi.org/10.1021/ez500267p).
- Ma, Q., H. Cheng, A.G. Fane, R. Wang, and H. Zhang. 2016. “Recent Development of Advanced Materials with Special Wettability for Selective Oil/Water Separation.” *Small.* 12, pp. 2186–2202.
- Marcos, B., C. Moresoli, J. Skorpova, and B. Vaughan. 2009. “CFD Modeling of a Transient Hollow Fiber Ultrafiltration System for Protein Concentration.” *J. Memb. Sci.* 337, pp. 136–144.
- Marjani, A., A. Baghdadi, and M. Ghadiri. 2016. “Mathematical Modeling of Humidification Process by Means of Hollow Fiber Membrane Contactor.” *Membr. Water Treat.* 7, pp. 297–311.
- Mat, N.C., Y. Lou, and G.G. Lipscomb. 2014. “Hollow Fiber Membrane Modules.” *Curr. Opin. Chem. Eng.* 4, pp. 18–24. doi:<http://dx.doi.org/10.1016/j.coche.2014.01.002>.

- Matijević, E. and B.A. Pethica. 1958. "The Properties of Ionized Monolayers. Part 1.—Sodium Dodecyl Sulphate at the Air/Water Interface." *Trans. Faraday Soc.* 54, pp. 1382–1389. doi:10.1039/TF9585401382.
- Maupin, M.A., J.F. Kenny, S.S. Hutson, J.K. Lovelace, N.L. Barber, and K.S. Linsey. 2014. *Estimated use of water in the United States in 2010*. U.S. Geological Survey, Reston, Virginia. doi:10.3133/cir1405.
- Mistry, K.H., R.K. McGovern, G.P. Thiel, E.K. Summers, S.M. Zubair, and J.H. Lienhard. 2011. "Entropy Generation Analysis of Desalination Technologies." *Entropy* 13, pp. 1829–1864. doi:10.3390/e13101829.
- Mistry, K.H. and J.H. Lienhard. 2013. "Generalized Least Energy of Separation for Desalination and Other Chemical Separation Processes." *Entropy* 15, pp. 2046–2080. doi:10.3390/e15062046.
- Neidhardt, H., S. Norra, X. Tang, H. Guo, and D. Stüben. 2012. "Impact of Irrigation with High Arsenic Burdened Groundwater on the Soil–Plant System: Results From a Case Study in the Inner Mongolia, China." *Environ. Pollut.* 163, pp. 8–13. doi:10.1016/J.ENVPOL.2011.12.033.
- Nejati, S., C. Boo, C.O. Osuji, and M. Elimelech. 2015. "Engineering Flat Sheet Microporous PVDF Films for Membrane Distillation." *J. Memb. Sci.* 492, pp. 355–363. doi:10.1016/J.MEMSCI.2015.05.033.
- Norra, S., Z.A. Berner, P. Agarwala, F. Wagner, D. Chandrasekharam, and D. Stüben. 2005. "Impact of Irrigation with As Rich Groundwater on Soil and Crops: a Geochemical Case Study in West Bengal Delta Plain, India." *Appl. Geochemistry* 20, pp. 1890–1906. doi:http://dx.doi.org/10.1016/j.apgeochem.2005.04.019.
- Oliva, A., M. Costa, and C.D.P. Segarra. 1991. "Numerical Simulation of Solar Collectors: the Effect of Nonuniform and Nonsteady State of the Boundary Conditions." *Sol. Energy* 47, pp. 359–373.
- Paxson, A.T., J.L. Yagüe, K.K. Gleason, and K.K. Varanasi. 2014. "Stable Dropwise Condensation for Enhancing Heat Transfer via the Initiated Chemical Vapor Deposition (iCVD) of Grafted Polymer Films." *Adv. Mater.* 26, pp. 418–423.
- Porter, M.C. 1989. *Handbook of Industrial Membrane Technology* (1989).
- Qtiashat, M.R. and F. Banat. 2013. "Desalination by Solar Powered Membrane Distillation Systems." *Desalination* 308, pp. 186–197.
- Qu, D., J. Wang, D. Hou, Z. Luan, B. Fan, and C. Zhao. 2009 "Experimental Study of Arsenic Removal by Direct Contact Membrane Distillation." *J. Hazard. Mater.* 163, pp. 874–879.
- Roy, S.B., L. Chen, E.H. Girvetz, E.P. Maurer, W.B. Mills, and T.M. Grieb. 2012. "Projecting Water Withdrawal and Supply for Future Decades in the U.S. under Climate Change Scenarios." *Environ. Sci. Technol.* 46, pp. 2545–2556. doi:10.1021/es2030774.

- Selmi, M., M.J. Al-Khawaja, and A. Marafia. 2008. "Validation of CFD simulation for Flat Plate Solar Energy Collector." *Renew. Energy* 33, pp. 383–387.
- Servi, A.T., J. Kharraz, D. Klee, K. Notarangelo, B. Eyob, E. Guillen-Burrieza, A. Liu, H.A. Arafat, and K.K. Gleason. 2016. "A Systematic Study of the Impact of Hydrophobicity on the Wetting of MD Membranes." *J. Memb. Sci.* 520, pp. 850–859. doi:10.1016/J.MEMSCI.2016.08.021.
- Shatat, M., M. Worall, and S. Riffat. 2013. "Opportunities for Solar Water Desalination Worldwide: Review." *Sustain. Cities Soc.* 9, pp. 67–80. doi:http://dx.doi.org/10.1016/j.scs.2013.03.004.
- Singh, G.K. 2013. "Solar Power Generation by PV (Photovoltaic) Technology: a Review." *Energy* 53, pp. 1–13. doi:http://dx.doi.org/10.1016/j.energy.2013.02.057.
- Sohrabi, M.R., A. Marjani, S. Moradi, M. Davallo, and S. Shirazian. 2011. "Mathematical Modeling and Numerical Simulation of CO₂ Transport Through Hollow-Fiber Membranes." *Appl. Math. Model.* 35, pp. 174–188.
- Souhaimi, M.K. and T. Matsuura. 2011. *Membrane Distillation: Principles and Applications*. Elsevier, 2011.
- Su, M., Y. Bai, J. Han, J. Chen, and H. Sun. 2018. "Adhesion of Gypsum Crystals to Polymer Membranes: Mechanisms and Prediction." *J. Memb. Sci.* 566, pp. 104–111. doi:10.1016/j.memsci.2018.08.062.
- Sun, S.P., T.A. Hatton, S.Y. Chan, and T.S. Chung. 2012. "Novel Thin-Film Composite Nanofiltration Hollow Fiber Membranes with Double Repulsion for Effective Removal of Emerging Organic Matters from Water." *J. Memb. Sci.* 401–402, pp. 152–162. doi:10.1016/j.memsci.2012.01.046.
- Teoh, M.M., S. Bonyadi, and T.-S.S. Chung. 2008. "Investigation of Different Hollow Fiber Module Designs for Flux Enhancement in the Membrane Distillation Process." *J. Memb. Sci.* 311, pp. 371–379. doi:10.1016/j.memsci.2007.12.054.
- Tomaszewska, M. 2015. "Sweep Gas Membrane Distillation (SGMD)." In *E. Drioli, L. Giorno (Eds.), Encycl. Membr., Springer Berlin Heidelberg, Berlin, Heidelberg*, pp. 1–3. doi:10.1007/978-3-642-40872-4_769-2.
- Tuteja, A., W. Choi, M. Ma, J.M. Mabry, S.A. Mazzella, G.C. Rutledge, G.H. McKinley, and R.E. Cohen. 2007. "Designing Superoleophobic Surfaces." *Science* 318, pp. 1618–22. doi:10.1126/science.1148326.
- Tuteja, A., W. Choi, G.H. McKinley, R.E. Cohen, and M.F. Rubner. 2008. "Design Parameters for Superhydrophobicity and Superoleophobicity." *MRS Bull.* 33, pp. 752–758. doi:10.1557/mrs2008.161.
- Upadhyaya, S., K. Singh, S.P. Chaurasia, R.K. Dohare, and M. Agarwal. 2016. "Mathematical and CFD Modeling of Vacuum Membrane Distillation for Desalination." *Desalin. Water Treat.* 57, pp. 11956–11971. doi:10.1080/19443994.2015.1048306.

- Villar, N.M., J.M.C. López, F.D. Muñoz, E.R. García, and A.C. Andrés. 2009. “Numerical 3-D Heat Flux Simulations on Flat Plate Solar Collectors.” *Sol. Energy* 83, pp. 1086–1092.
- Wang, X.A. and L.G. Wu. 1990. “Analysis and Performance of Flat-Plate Solar Collector Arrays.” *Sol. Energy* 45, pp. 71–78.
- Wang, K.Y., T.-S.S. Chung, and M. Gryta. 2008. “Hydrophobic PVDF Hollow Fiber Membranes with Narrow Pore Size Distribution and Ultra-Thin Skin for the Fresh Water Production through Membrane Distillation.” *Chem. Eng. Sci.* 63, pp. 2587–2594. doi:10.1016/j.ces.2008.02.020.
- Wang, Z., Y. Chen, and S. Lin. 2018. “Kinetic Model for Surfactant-Induced Pore Wetting in Membrane Distillation.” *J. Memb. Sci.* 564, pp. 275–288. doi:10.1016/J.MEMSCI.2018.07.010.
- Warsinger, D., K. Mistry, K. Nayar, H. Chung, J. Lienhard V. 2015. “Entropy Generation of Desalination Powered by Variable Temperature Waste Heat.” *Entropy* 17, pp. 7530–7566. doi:10.3390/e17117530.
- Yan, Y., Z. Zhang, L. Zhang, Y. Chen, and Q. Tang. 2014. “Dynamic Modeling of Biogas Upgrading in Hollow Fiber Membrane Contactors.” *Energy & Fuels* 28, 5745–5755.
- Yang, X., R. Wang, and A.G. Fane. 2011. “Novel Designs for Improving the Performance of Hollow Fiber Membrane Distillation Modules.” *J. Memb. Sci.* 384, pp. 52–62. doi:http://dx.doi.org/10.1016/j.memsci.2011.09.007.
- Yarlagadda, S., V.G. Gude, L.M. Camacho, S. Pinappu, and S. Deng. 2011. “Potable Water Recovery from As, U, and F Contaminated Ground Waters by Direct Contact Membrane Distillation Process.” *J. Hazard. Mater.* 192, pp. 1388–1394.
- Yaws, C.L. 2005. *The Yaws Handbook of Vapor Pressure : Antoine Coefficients*. Elsevier, 2005.
- Zheng, J., Y. Xu, and Z. Xu. 2003. “Flow Distribution in a Randomly Packed Hollow Fiber Membrane Module.” *J. Memb. Sci.* 211, pp. 263–269. doi:10.1016/S0376-7388(02)00426-X.
- Zhu, J., X. Lu, R. Balieu, and N. Kringos. 2016. “Modelling and Numerical Simulation of Phase Separation in Polymer Modified Bitumen by Phase-Field Method.” *Mater. Des.* 107, pp. 322–332. doi:http://dx.doi.org/10.1016/j.matdes.2016.06.041.
- Zuo, J., S. Bonyadi, and T.-S. Chung. 2016. “Exploring the Potential of Commercial Polyethylene Membranes for Desalination by Membrane Distillation.” *J. Memb. Sci.* 497, pp. 239–247.

Metric Conversions

Unit	Metric equivalent
1 gallon	3.785 liters
1 gallon per minute	3.785 liters per minute
1 gallon per square foot of membrane area per day	40.74 liters per square meter per day
1 inch	2.54 centimeters
1 million gallons per day	3,785 cubic meters per day
1 pound per square inch	6.895 kilopascals
1 square foot	0.093 square meters
°F (temperature measurement)	$(^{\circ}\text{F}-32) \times 0.556 = ^{\circ}\text{C}$
1°F (temperature change or difference)	0.556°C

This page intentionally left blank.

Appendix A

Mathematical Modeling of Hollow Fiber Membrane Packing Configurations

Computational Domain

Membrane distillation using hollow fiber modules includes transport phenomena in three computational domains: module shell, membrane lumen, and membrane body. Here, we assume the warm saline stream (feed) flows in the shell of the module. Also, depending on the mode of operation, either a cold freshwater stream (DCMD) or an air stream (SGMD) flows in the hollow fiber membrane's (HFM's) lumen. The porous membrane body acts as a solid physical barrier between the mentioned streams that only allows water vapor and heat transfer. In the following, the governing equations for DCMD and SGMD are defined in detail.

Fluid flow

Feed and Distillate/Air

The Navier-Stokes and continuity equations for fluid flow within the feed and distillate/air streams can be written as:

$$\nabla \cdot (\rho \bar{u} \bar{u}) = -\nabla p + \mu \nabla \cdot \left[\left(\nabla \bar{u} + \nabla (\bar{u})^T \right) \right] + \rho g \quad (A1)$$

$$\nabla \cdot (\rho \bar{u}) = 0 \quad (A2)$$

where ρ and μ are the density and viscosity of the corresponding fluid, g is the acceleration due to gravity; and \bar{u} and p are velocity vector and pressure, respectively. The boundary conditions for solving momentum and continuity equations in the feed and distillate/air streams are non-slip flow on the membrane surface, symmetric flow at the symmetry boundaries, constant velocity at the inlet boundaries, and gauge pressure at the outlet boundaries.

Porous Membrane

To define a flow field in the porous membrane and consider the effect of total pressure difference on transmembrane transport phenomena, we applied Darcy's law, defined as:

$$\bar{u} = \frac{-B_0}{\mu} \nabla P \quad (A3)$$

where B_0 is the permeability of the porous membrane, defined using the following correlation (Lee et al. 2014):

$$B_0 = \frac{\varepsilon d_p^2}{32} \quad (\text{A4})$$

where ε and d_p are the averaged porosity and pore size, respectively, of the HFM. The boundary conditions for solving Darcy's equation (Equation A3) in the membrane domain was defined as the total pressure at each interface.

Heat Transfer

Feed and Distillate/Air Streams

Heat transfer within the feed and distillate/air domains was defined using equations (A5) and (A6):

$$\rho C_p \vec{u} \cdot \nabla T = \nabla q \quad (\text{A5})$$

$$\nabla q = -k \nabla T \quad (\text{A6})$$

where k and C_p are the thermal conductivity and heat capacity of the corresponding stream, respectively. The boundary conditions for the flow streams were as follows:

Feed stream

$$T = T_{f,m} \quad \text{Feed-membrane interface} \quad (\text{A7})$$

$$\nabla T = 0 \quad \text{Symmetry planes } S_1-S_6 \quad (\text{A8})$$

$$T = T_{f,in} \quad \text{Feed inlet} \quad (\text{A9})$$

$$\nabla T = 0 \quad \text{Feed outlet} \quad (\text{A10})$$

where $T_{f,m}$ and $T_{f,in}$ are the membrane (membrane-feed interface) and feed inlet temperatures, respectively.

Distillate/Airstream

$$T = T_{m,l} \quad \text{Membrane-distillate/air interface} \quad (\text{A11})$$

$$\nabla T = 0 \quad \text{Center of the lumen } (r=0) \quad (\text{A12})$$

$$T = T_{i,in} \quad \text{Distillate/air inlet} \quad (\text{A13})$$

$$\nabla T = 0 \quad \text{Distillate/air outlet} \quad (\text{A14})$$

where, $T_{i,in}$ is the inlet distillate/air temperature.

Porous membrane

It was assumed that the heat is transferred through conduction. Thus, equation (A5) is simplified to:

$$-k_m \nabla T_m = 0 \quad (A15)$$

where k_m is the thermal conductivity of the membrane. The boundary conditions for the membrane are as follows:

SGMD

$$-k_m \nabla T = J_w \Delta H_{vap,w} - h_f (T_{f,bulk} - T) \quad \text{Feed-membrane interface} \quad (A16)$$

$$-k_m \nabla T = J_w C_{p,s} T - h_a (T_{a,bulk} - T) \quad \text{Air-membrane interface} \quad (A17)$$

$$\nabla T = 0 \quad \text{Two ends of the hollow fiber} \quad (A18)$$

where J_w is the molar flux of water vapor across the respective interface, and $\Delta H_{vap,w}$ is the heat of vaporization of water. Here, h_f and h_a are the convective heat transfer coefficients of the flow streams determined using Nusselt correlations; and $T_{f,bulk}$ and $T_{a,bulk}$ are the bulk temperatures of the feed and air streams, respectively, calculated by averaging the temperature of points furthest away from the membrane boundary. Also, $C_{p,s}$ is the heat capacity of steam (vapor) added to the air stream.

DCMD

The only change in the boundary conditions at the distillate side, equation (A17), considering the condensation of water at the distillate interface:

$$-k_m \nabla T = J_w \Delta H_{vap,w} - h_d (T_{d,bulk} - T) \quad \text{Feed-membrane interface} \quad (A19)$$

The convective heat transfer coefficients (h_f and h_d) can be determined using the following equation:

$$h = \frac{\text{Nu } k}{D_H} \quad (A18)$$

where D_H is the hydraulic diameter and Nu is the Nusselt number, calculated using equations (A20) and (A21) for the feed (in the shell) and distillate (in the lumen). For water streams with a

Reynolds number between 40 and 2,100, the following empirical equations were used to estimate Nu numbers (Teoh et al. 2008):

$$\text{Nu}_f = 0.042 \text{Re}_f^{0.59} \text{Pr}_f^{0.33} \quad (\text{A19})$$

$$\text{Nu}_d = 1.86 \left(\frac{d_i}{L} \text{Re}_d \text{Pr}_d \right)^{0.33} \quad (\text{A20})$$

Mass Transfer

Water vapor transfer inside the membrane

The mass transfer model for gas molecules diffusing through a porous medium can be described using four primary mechanisms: Knudsen diffusion, molecular diffusion, viscous flow, and surface diffusion. The effect of surface diffusion on overall mass transfer can be ignored because the membranes are made of hydrophobic polymeric materials (Lee and Karnik 2010; Giaya and Thompson 2002). Thus, the diffusion of gas molecules in a porous medium can be modeled using the dusty-gas model which is the combination of diffusional regimes -- molecular, Knudsen, and viscous flow (Deshmukh and Lee 2019).

The general dusty gas model for a multicomponent diffusion of species in porous media can be written as:

$$\sum_{\substack{j=1 \\ j \neq i}}^n \frac{x_j \bar{N}_i - x_i \bar{N}_j}{D_{ij}} + \frac{\bar{N}_i}{D_{iM}} = -\frac{P_t}{RT} \nabla x_i + \frac{x_i}{RT} \left(1 + \frac{B_0 P_t}{\mu D_{iM}} \right) \nabla P_t \quad (\text{A21})$$

where x_i and x_j are the mole fraction of component i and j, respectively. D_{ij} is the effective molecular diffusion coefficient of component i in j and D_{iM} is the effective Knudsen diffusion coefficient of component 'i' in the porous media.

To simplify the dusty-gas model for MD, the following assumptions were considered:

- The gas mixture is binary (air and water vapor) and behaves as an ideal gas.
- The air within the membrane is considered stagnant.

Considering a binary mixture, the dusty-gas model will be simplified to the diffusion of water vapor inside stagnant air trapped in the porous membrane:

$$\frac{\bar{N}_w}{D_{eff}} = -\frac{P_t}{RT} \nabla x_w - \frac{x_w}{RT} \left(1 + \frac{B_0 P_t}{\mu D_{wM}} \right) \nabla P_t \quad (\text{A22})$$

$$D_{eff} = \frac{\varepsilon}{\tau} \left(\frac{1-x_w}{D_{wa}} + \frac{1}{D_{wM}} \right)^{-1} \quad (\text{A23})$$

where x_w , D_{eff} , D_{wa} , D_{wM} , T , and τ are the mole fraction of water vapor in the pores, effective diffusion coefficient, the molecular diffusion coefficient of water vapor in the air, Knudsen diffusion coefficient of water vapor, membrane temperature, and tortuosity, respectively.

D_{wa} and D_{wM} can be defined as following (Kast and Hohenthanner 2000; Li and Sirkar 2016):

$$D_{wa} [m^2 s^{-1}] = \frac{1.895 \times 10^{-5} T^{2.072}}{P_t} \quad 0^\circ C < T < 100^\circ C \quad (A24)$$

$$D_{wM} [m^2 s^{-1}] = \frac{4d_p}{3} \sqrt{\frac{RT}{2\pi M_w}} \quad (A25)$$

The mole fraction of water, x_w , can be approximated using the saturation vapor pressure of water, which is a function of temperature, total pressure, and water salinity:

$$x_w = \frac{p_w^{sat}(T, P_t, x_{NaCl})}{P_t} \quad (A26)$$

where $p_w^{sat}(T, P_t, x_{NaCl})$ is the saturation pressure of water across the membrane calculated by the Kohler theory that takes into account the effect of osmotic and total pressure on vapor pressure (Deshmukh and Lee 2019):

$$p_w^{sat}(T, P_t, x_{NaCl}) = p_{0,w}^{sat} \exp\left[\frac{(P_t - \Pi)v_m}{RT}\right] \quad (A27)$$

where p_0^{sat} is the vapor pressure of pure water determined by Antoine's equation and Π is the osmotic pressure at a given concentration. Here, v_m is the molar volume of water. Accordingly, $p_{0,w}^{sat}$ can be determined using Antoine's equation:

$$p_{0,w}^{sat} [kPa] = \gamma_w \exp\left(A - \frac{B}{C + T [^\circ C]}\right) \quad (A28)$$

A, B, and C are Antoine's constants for water and are equal to 16.3872, 3885.70, and 230.17, respectively (Yaws 2005). Here, γ_w is the activity coefficient of water in an aqueous sodium chloride solution, defined using the following empirical equation for the sodium chloride concentration from zero to saturation at a temperature range between 30 °C and 100 °C (Lawson 1997):

$$\gamma_w = 1 - 0.5x_{NaCl} - 10x_{NaCl}^2 \quad (A29)$$

where x_{NaCl} is the molar fraction of the salt in water.

The boundary conditions for solving the mass transfer equation within the membrane are as follows:

DCMD Configuration

$$c_w = \frac{(1 - x_{NaCl}) P_{0,w}^{sat}}{RT} \quad \text{Feed-membrane interface} \quad (A30)$$

$$c_w = \frac{P_{0,w}^{sat}}{RT} \quad \text{Distillate-membrane interface} \quad (A31)$$

$$\frac{dc_w}{dz} = 0 \quad \text{Two ends of the hollow fiber} \quad (A32)$$

SGMD Configuration

For SGMD, all mass transfer boundary conditions inside the membrane are the same as DCMD configuration except the distillate/air interface boundary condition that changes to:

$$N_w = Sh \frac{D_{wa}}{2R_i} (c_{w,bulk} - c_w) \quad (A33)$$

where Sh and R_i are the Sherwood number and inner radius of the HFM, respectively. The Sherwood number for a laminar flow inside the lumen of hollow fiber can be defined as:

$$Sh = 1.86 Re^{0.8} / \quad (A34)$$

where Re is the Reynolds number for laminar flow within a tubular geometry.

Water vapor transfer in air

The following equations can capture the mass transfer within the air stream in SGMD configuration:

$$\nabla \cdot (J_w) + u \cdot \nabla c_w = 0 \quad (A35)$$

$$J_w = -D_{wa} \nabla c_w \quad (A36)$$

where D_{wa} is the molecular diffusion coefficient of water in the air (determined using equation A24) and c_w is the concentration of water in the air. The boundary conditions for solving the mass transfer equations in the air stream inside the lumen are as follows:

$$c_w = \varepsilon c_{w,a} \quad \text{Air-Membrane interface} \quad (A37)$$

$$c_w = c_{w,in} \quad \text{Air inlet} \quad (A38)$$

$$\nabla c_w = 0 \quad \text{Air outlet} \quad (\text{A39})$$

$$\nabla c_w = 0 \quad \text{Symmetry planes} \quad (\text{A40})$$

where $c_{w,a}$ is the concentration of water in the membrane, and ε is the membrane surface porosity. The effective physical properties of the air-water mixture (χ_{mix}), such as density, viscosity, and heat capacity, were estimated using the following equation:

$$\chi_{\text{mix}} = (1 - x_w) \chi_a + x_w \chi_w \quad (\text{A41})$$

where χ_a and χ_w are the physical properties of the water vapor and air, respectively.

This page intentionally left blank.

Appendix B

Formulation of Governing Thermodynamic Equations

Figure B-1 illustrates a black box separator with incoming seawater stream and outflowing product and brine streams. The separator takes in solar power rejects some of that power due to thermal inefficiencies. The control volume in Figure B-1 was selected in the distance far from the desalination plant such that the inlet and outlet streams are in equilibrium with the environment. The logic behind this selection is that the purpose of a desalination plant is to produce water and not heated water. Any stream that is at a higher temperature than the temperature of the environment will lose its heat, which contributes to entropic losses to the system.

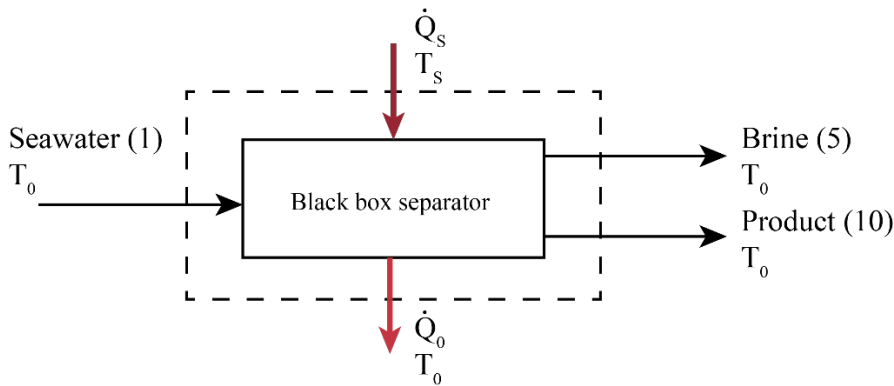


Figure B-1. Block flow diagram (straight line) with a control volume (dashed line) on the black box separator. The control volume is selected in the distance far from the desalination plant such that the inlet and outlet streams are in equilibrium with the environment. The number of streams corresponds to streams in Figure 5.

Applying the first and second law on control volume in Figure B-1 yields (Warsinger et al. 2015):

$$\dot{Q}_s - \dot{Q}_0 = (\dot{m}h)_{10} + (\dot{m}h)_5 - (\dot{m}h)_1 \quad (B1)$$

$$\frac{\dot{Q}_s}{T_s} - \frac{\dot{Q}_0}{T_0} = (\dot{m}s)_{10} + (\dot{m}s)_5 - (\dot{m}s)_1 + \dot{S}_{gen} \quad (B2)$$

Combining Equations (B1) and (B2) and using the relations $g = h - T_s$ and $R = m_{10}/m_1$

$$\frac{\dot{Q}_s}{\dot{m}_{10}} \left(1 - \frac{T_0}{T_s} \right) = (g_{10} - g_5) - \frac{1}{R} (g_1 - g_5) + \frac{T_0 \dot{S}_{gen}}{\dot{m}_{10}} \quad (B3)$$

The reversible heat which is also referred to as the least heat of separation is defined by:

$$\frac{\dot{Q}_{least}}{\dot{m}_{10}} \left(1 - \frac{T_0}{T_S} \right) = (g_{10} - g_5) - \frac{1}{R} (g_1 - g_5) \quad (B4)$$

The second law efficiency for a thermal driven desalination process is defined as:

$$\eta_{II} = \frac{\dot{Q}_{least}^{\min}}{\dot{Q}_S} = \frac{\dot{Q}_{least}^{\min}}{\dot{Q}_{least} + \left(1 - \frac{T_0}{T_S} \right)^{-1} T_0 \dot{S}_{gen}} \quad (B5)$$

Where the minimum least heat of separation is defined as:

$$\dot{Q}_{least}^{\min} \equiv \lim_{R \rightarrow 0} \dot{Q}_{least} \quad (B6)$$

Applying the first and second law of thermodynamics to the DCMD module (Equations (B7) and (B8)), heat exchanger (Equations (B9) and (B10)), solar collector (Equations (B11) and (B12)) Bejan et al. 1981), and cooler (Equations (B13) and (B14)) in Figure 5:

$$\dot{m}_4 c_p (T_4 - T_5) + \dot{m}_6 c_p (T_6 - T_7) + \dot{m}_{10} c_p (T_5 - T_7) = 0 \quad (B7)$$

$$\dot{m}_4 c_p \ln \left(\frac{T_5}{T_4} \right) + \dot{m}_6 c_p \ln \left(\frac{T_7}{T_6} \right) + \dot{m}_{10} c_p \ln \left(\frac{T_6}{T_8} \right) = \dot{S}_{gen}^{DCMD} \quad (B8)$$

$$\dot{m}_7 c_p (T_8 - T_7) + \dot{m}_2 c_p (T_3 - T_2) = 0 \quad (B9)$$

$$\dot{m}_7 c_p \ln \left(\frac{T_8}{T_7} \right) + \dot{m}_2 c_p \ln \left(\frac{T_3}{T_2} \right) = \dot{S}_{gen}^{HEX} \quad (B10)$$

$$\dot{m}_3 c_p (T_4 - T_3) - \dot{Q}_S + \dot{Q}_0 = 0 \quad (B11)$$

$$\dot{m}_3 c_p \ln \left(\frac{T_4}{T_3} \right) - \frac{\dot{Q}_S}{T_S} + \frac{\dot{Q}_0}{T_0} = \dot{S}_{gen}^{SC} \quad (B12)$$

$$\dot{m}_{11} c_p (T_{11} - T_6) - \dot{Q}_{cooler} = 0 \quad (B13)$$

$$\dot{m}_{11} c_p \ln \left(\frac{T_{11}}{T_6} \right) - \frac{\dot{Q}_{cooler}}{T_{cooler}} = \dot{S}_{gen}^{cooler} \quad (B14)$$

Streams 5 and 10 lose their energy to the environment, which leads to entropy generation. The entropy generation rate can be found using (Warsinger et al. 2015; Mistry et al. 2011; Mistry et al. 2013; Lienhard et al. 2017):

$$\dot{S}_{gen}^{disequilibrium} = \dot{m}_5 c_p \left[\ln \left(\frac{T_0}{T_5} \right) + \frac{T_5}{T_0} - 1 \right] + \dot{m}_{10} c_p \left[\ln \left(\frac{T_0}{T_{10}} \right) + \frac{T_{10}}{T_0} - 1 \right] \quad (B15)$$

Total entropy generation is the sum of all entropy generation:

$$\dot{S}_{gen}^{total} = \dot{S}_{gen}^{DCMD} + \dot{S}_{gen}^{HEX} + \dot{S}_{gen}^{SC} + \dot{S}_{gen}^{cooler} + \dot{S}_{gen}^{disequilibrium} \quad (B16)$$

Specific entropy generation is the entropy generation is defined as the entropy generated per unit of water produced:

$$\zeta_{gen} = \frac{\dot{S}_{gen}}{\dot{m}_{10}} \quad (B17)$$

This page intentionally left blank.

Appendix C

Procedure for Assembling Reentrant Structures on Hollow Fiber Membranes

To make anti-wetting hollow fiber membranes (HFMs) having reentrant structures on their outer surface, we first fabricated HFMs using the dry-jet wet-spinning method. The detailed processing condition for making pristine HFMs can be found in Subtask 3.1. The pristine and vacuum-dried HFMs were transferred to the initiated chemical vapor deposition (iCVD) reactor on a custom-made holder. Subsequently, we deposited two low-surface energy polymers, polytetrafluoroethylene (PTFE) and poly (perfluoro decyl acrylate), PPFDA, on the outer surface on HFMs in two consecutive steps illustrated in Figure C-1. In the first step, we assembled random reentrant structures of PTFE on the outer surfaces of HFMs. The process conditions were adjusted such that the deposition is diffusion-limited, creating a random porous structure of PTFE. In the second step, without breaking the vacuum of the iCVD reactor, we rendered the reentrant structures omniphobic by grafting a highly fluorinated polymer, PPFDA, on the PTFE structures.

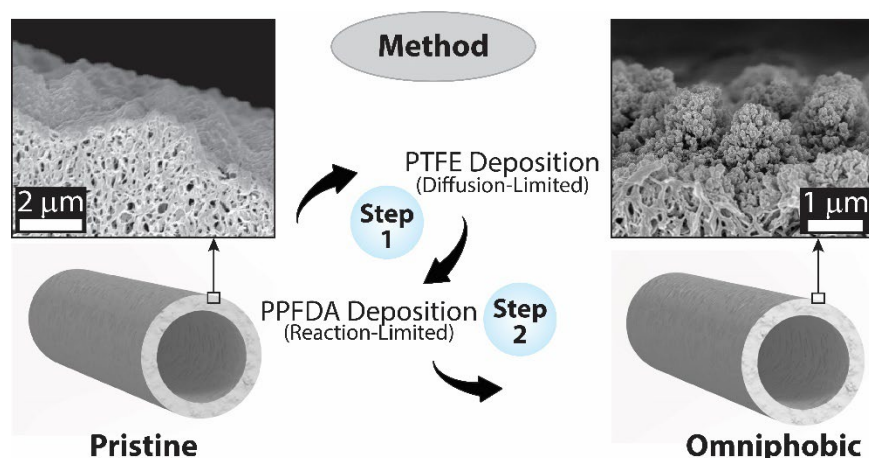


Figure C-1. Schematic of procedures used to fabricate omniphobic HFMs through a sequential initiated chemical vapor deposition (iCVD) method

This page intentionally left blank.